The Interaction between the Supernova Remnant W41 and the Filamentary Infrared Dark Cloud G23.33-0.30

Taylor G. Hogge[1] , James M. Jackson[1,2,3] , David Allingham[3], Andres E. Guzman[4] , Nicholas Killerby-Smith[3], Kathleen E. Kraemer[5] , Patricio Sanhueza[4] , Ian W. Stephens[6] , and J. Scott Whitaker[7]

[1] Institute for Astrophysical Research, 725 Commonwealth Ave., Boston University, Boston, MA 02215, USA; thogge@bu.edu
[2] SOFIA Science Center, USRA, NASA Ames Research Center, Moffett Field CA 94045, USA
[3] School of Mathematical and Physical Sciences, University of Newcastle, University Drive, Callaghan NSW 2308, Australia
[4] National Astronomical Observatory of Japan, National Institutes of Natural Sciences, 2-21-1 Osawa, Mitaka, Tokyo 181-8588, Japan
[5] Institute for Scientific Research, Boston College, 140 Commonwealth Avenue, Chestnut Hill, MA 02467, USA
[6] Harvard-Smithsonian Center for Astrophysics, 60 Garden Street, Cambridge, MA 02138, USA
[7] Physics Department, 590 Commonwealth Ave., Boston University, Boston, MA 02215, USA
Received 2019 August 27; revised 2019 October 22; accepted 2019 October 24; published 2019 December 12

Abstract

G23.33-0.30 is a 600 $M_\odot$ infrared dark molecular filament that exhibits large NH_3 velocity dispersions ($\sigma \sim 8\,km\,s^{-1}$) and bright, narrow $NH_3(3, 3)$ line emission. We have probed G23.33-0.30 at the < 0.1 pc scale and confirmed that the narrow $NH_3(3, 3)$ line is emitted by four rare $NH_3(3, 3)$ masers, which are excited by a large-scale shock impacting the filament. G23.33-0.30 also displays a velocity gradient along its length, a velocity discontinuity across its width, shock-tracing SiO(5–4) emission extended throughout the filament, and broad turbulent line widths in $NH_3(1, 1)$ through (6, 6), CS(5–4), and SiO(5–4), as well as an increased NH_3 rotational temperature (T_{rot}) and velocity dispersion (σ) associated with the shocked, blueshifted component. The correlations among T_{rot}, σ, and V_{LSR} imply that the shock is accelerating, heating, and adding turbulent energy to the filament gas. Given G23.33-0.30's location within the giant molecular cloud G23.0-0.4, we speculate that the shock and $NH_3(3, 3)$ masers originated from the supernova remnant (SNR) W41, which exhibits additional evidence of an interaction with G23.0-0.4. We have also detected the 1.3 mm dust continuum emission from at least three embedded molecular cores associated with G23.33-0.30. Although the cores have moderate gas masses ($M = 7$–10 $M_\odot$), their large virial parameters ($\alpha = 4$–9) suggest that they will not collapse to form stars. The turbulent line widths of the ($\alpha > 1$) cores may indicate negative feedback due to the SNR shock.

Unified Astronomy Thesaurus concepts: Supernova remnants (1667); Infrared dark clouds (787)

1. Introduction

High-mass stars ($M > 8\,M_\odot$), though rare, have a profound impact on the evolution of the interstellar medium (ISM). Throughout their short lifetimes ($\sim 10^6$ yr), high-mass stars will release fast, radiation-driven stellar winds that carve H II regions into the surrounding molecular clouds (MCs). High-mass stars end their lives by releasing $\sim 10^{51}$ erg of energy near-instantaneously in the form of supernovae (SNe). Shocks from expanding H II regions and supernova remnants (SNRs) accelerate, heat, and add turbulence to their surrounding gas. While these feedback mechanisms are thought to play a significant role in regulating the star formation process, the exact role these shocks play is not yet well-understood. The results from hydrodynamic simulations of SNR–MC interactions differ depending on specific parameters, but they show that such interactions could potentially aid or inhibit star formation. Some models suggest that shocks act to disperse dense gas structures (Pittard & Parkin 2016). On the other hand, because postshock gas is compressed, other models suggest that this shock-induced compression can trigger collapse to form even denser compact structures (Orlando et al. 2005). Because the influence of SNe on the star formation process has implications for galaxy evolution, it is important to gain a better understanding of SNR–MC interactions. The sites of these interactions can be associated with broad molecular line widths (Reach et al. 2005) and shock-excited maser emission in the 1720 MHz OH transition (Wardle & Yusef-Zadeh 2002) and the $NH_3(3, 3)$ inversion transition (McEwen et al. 2016).

Dense molecular gas structures that exhibit evidence of broad molecular line widths, 1720 MHz OH maser emission, or NH3 (3, 3) maser emission, but lack an obvious stellar source, are prime targets to investigate potential SNR–MC interactions.

G23.33-0.30 is a dense molecular filament with extremely broad molecular line widths. Due to the lack of any evidence at infrared wavelengths for embedded star formation, these broad line widths are puzzling. The H_2O Southern Galactic Plane Survey (HOPS; Walsh et al. 2011) detected extremely broad NH_3 line widths and a bright, narrow feature in the $NH_3(3, 3)$ line profile toward G23.33-0.30. Figure 1 displays Radio Ammonia Mid-Plane Survey (RAMPS; Hogge et al. 2018) $NH_3(1, 1)$ through (4, 4) spectra toward G23.33-0.30 at an angular resolution ($\theta \sim 32''$) higher than that of HOPS ($\theta \sim 120''$). The spectra show the uncommonly broad line emission associated with G23.33-0.30, as well as emission from an unrelated background MC with a local standard of rest (LSR) velocity of $V_{LSR} = 103\,km\,s^{-1}$ that exhibits more typical NH_3 line profiles. G23.33-0.30's molecular line emission has a large velocity dispersion ($\sigma \sim 8\,km\,s^{-1}$), much larger than that of a typical dense MC ($\sigma \sim 0.5$–3 $km\,s^{-1}$; Sanhueza et al. 2012). Moreover, the $NH_3(3, 3)$ spectrum displays a bright, narrow line component superposed on a fainter, broad component. Unlike the broad component, the bright, narrow line emission in the ortho ($K = 3n$) $NH_3(3, 3)$ spectrum has no corresponding component in the para ($K \neq 3n$) transitions. Because masers emit at such small spatial scales (e.g., Elitzur 1992), the single-dish observations lack the
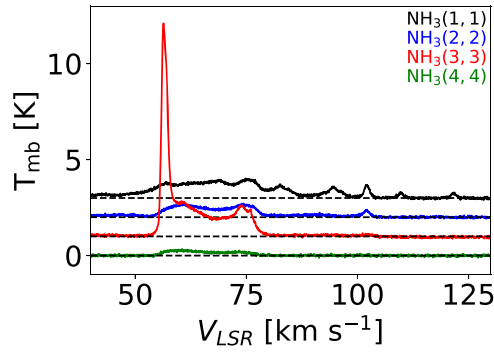
Figure 1. RAMPS $NH_3(1, 1)$ through $(4, 4)$ spectra toward the peak of the narrow $NH_3(3, 3)$ emission. The broad emission from G23.33-0.30 is centered near $V_{LSR} = 67\ km\ s^{-1}$, while the more typical NH_3 emission from a presumably unrelated source peaks at $V_{LSR} = 103\ km\ s^{-1}$. The emission from G23.33-0.30 exhibits extremely broad line widths, enhanced $NH_3(3, 3)/(1, 1)$ brightness temperature ratio, and an $NH_3(3, 3)$ maser candidate.

Table 1
Known $NH_3(3, 3)$ Masers

Source	Flux (Jy)	Reference
DR21(OH)	0.260	Mangum & Wootten (1994)
W51	0.230	Zhang & Ho (1995)
NGC 6334 V	0.114	Kraemer & Jackson (1995)
NGC 6334 I	0.482	Kraemer & Jackson (1995)
IRAS 20126+4104	0.079	Zhang et al. (1999)
G5.89-0.39	0.031	Hunter et al. (2008)
G20.08-0.14N	0.191	Galván-Madrid et al. (2009)
G23.33-0.30	9.7	Walsh et al. (2011)
G30.7206-00.0826	5	Urquhart et al. (2011)
G35.03+0.35	0.065	Brogan et al. (2011)
G28.34+0.06	0.03	Wang et al. (2012)
W51C	1.4	McEwen et al. (2016)
W44	0.07	McEwen et al. (2016)
G5.7-0.0	0.35	McEwen et al. (2016)
G1.4-0.1	0.58	McEwen et al. (2016)

angular resolution necessary to definitively determine whether the brightness temperature of this narrow feature is large enough to confirm maser emission. Nevertheless, the narrow line width of this component and its appearance solely in the $NH_3(3, 3)$ spectrum suggest that it is from an $NH_3(3, 3)$ maser. Compared to other masing transitions, $NH_3(3, 3)$ masers are exceedingly rare. Indeed, to our knowledge, only 15 sources with $NH_3(3, 3)$ masers have been discovered outside of the Galactic Center (Table 1). Although our understanding of $NH_3(3, 3)$ maser excitation is incomplete, studies have found that they can be excited by shocks resulting from SNR–MC interactions (McEwen et al. 2016) or energetic outflows from high-mass protostars (Mangum & Wootten 1994; Kraemer & Jackson 1995; Zhang & Ho 1995). While the majority of $NH_3(3, 3)$ masers have fluxes of $\lesssim 1$ Jy, Walsh et al. (2011) measured a flux of 9.7 Jy for G23.33-0.30's maser candidate, potentially making it the brightest yet detected. The unusually broad line widths may indicate that G23.33-0.30 is experiencing a particularly extreme impact from either an SNR or a high-mass protostellar outflow.

G23.33-0.30's broad NH_3 line emission is associated with a filamentary infrared dark cloud (IRDC) that resides within the giant molecular cloud (GMC) G23.0-0.4, a large ($\sim$84 × 15 pc), massive ($\sim 5 \times 10^5\ M_\odot$), and dense ($\sim 10^3\ cm^{-3}$) filamentary GMC (Su et al. 2015) that hosts multiple generations of high-mass star formation (Messineo et al. 2014). In particular, there are several nearby SNRs projected against G23.0-0.4, two of which, G22.7-0.2 (Su et al. 2014) and W41 (Frail et al. 2013; Su et al. 2015), may be interacting with the GMC. Furthermore, W41 exhibits 20 cm continuum emission, two 1720 MHz OH maser candidates, and extended TeV emission coincident with or adjacent to G23.33-0.30. G23.33-0.30's large peak H_2 column density of $N_{H_2} = 1.2 \times 10^{23}\ cm^{-2}$ (Peretto et al. 2016) is similar to that of other high-mass IRDCs, which are thought to be the formation sites of high-mass stars and stellar clusters (Rathborne et al. 2006). The Co-Ordinated Radio "N" Infrared Survey for High-mass star formation's (CORNISH; Hoare et al. 2012) nondetection of an H II region likely indicates that any high-mass stars forming within G23.33-0.30 are in an embedded prestellar or protostellar phase. Considering GMC G23.0-0.4's potential involvement in an SNR–MC interaction, as well as G23.33-0.30's potential capacity for high-mass star formation, stellar outflows or an SNR–MC interaction both remain viable

explanations for the excitation of the potential $NH_3(3, 3)$ maser emission.

To confirm the suspected $NH_3(3, 3)$ maser emission, determine its excitation conditions, and investigate the nature of the broad NH_3 line widths, we have performed follow-up observations of G23.33-0.30 that probe the filament at the <0.1 pc scale. In this paper, we present Karl G. Jansky Very Large Array (VLA) observations of the $NH_3(1, 1)$ through (6, 6) inversion lines, Atacama Compact Array (ACA) observations of the SiO(5–4), CS(5–4), and 1.3 mm continuum, and Submillimeter Array[8] (SMA) observations of the $^{13}CO(2–1)$, $C^{18}O(2–1)$, and 1.3 mm continuum. In Section 2, we describe these observations and the reduction of the data. In Section 3, we present the results. In Section 4, we analyze the data. In Section 5, we discuss the analysis. In Section 6, we provide our conclusions.

2. Observations and Data Reduction

We have observed G23.33-0.30 using the VLA, operated by the National Radio Astronomy Observatory,[9] the ACA, and the SMA. Table 2 provides a summary of the continuum and spectral line data analyzed in this work and Sections 2.1–2.3 describe the calibration and reduction of these data. We also display archival data from several surveys, which are summarized in Table 3.

2.1. VLA Observations

We observed G23.33-0.30 using the VLA in the D array configuration for a seven-hour track. We performed the bandpass and flux calibration of the data using observations of J1331+305 (3C286) and we performed the phase calibration using periodic observations of J1851+0035. The calibration and imaging of the data were performed using CASA[10] 5.1.1-5,

---

Table 2
New Observations

Telescope	Date	Transition	ν_0 (GHz)	θ_P (arcmin)	$\theta_{maj} \times \theta_{min}$ (arcsec)	ΔV_{BW} (km s^{-1})	ΔV_{chan} (km s^{-1})	σ_{noise} (mJy beam^{-1})
SMA	2016 Jun 20	$^{13}CO(2–1)$	220.39868	0.8	4.1×2.2	345	0.17	82.5
⋯	⋯	$C^{18}O(2–1)$	219.56035	0.8	4.1×2.2	173	0.17	92.0
⋯	⋯	1.3 mm cont.	⋯	0.8	4.1×2.2	10435	⋯	1.1
VLA-A	2016 Oct 7	$NH_3(3, 3)$	23.87013	1.9	0.13×0.09	50	0.39	8.1
VLA-D	2017 Apr 14	$NH_3(1, 1)$	23.69450	1.9	3.8×2.7	51	0.40	1.6
⋯	⋯	$NH_3(2, 2)$	23.72263	1.9	3.7×2.7	51	0.39	1.3
⋯	⋯	$NH_3(3, 3)$	23.87013	1.9	3.7×2.7	50	0.39	0.6
⋯	⋯	$NH_3(4, 4)$	24.13942	1.9	3.4×2.6	50	0.39	1.4
⋯	⋯	$NH_3(5, 5)$	24.53299	1.8	3.4×2.6	49	0.38	1.1
⋯	⋯	$NH_3(6, 6)$	25.05603	1.8	3.3×2.6	48	0.37	1.6
ACA	2017 Jul 10–13	$SiO(5–4)$	217.10498	0.8	7.2×4.5	689	0.34	20.2
⋯	⋯	1.3 mm cont.	⋯	0.8	6.6×4.0	5451	⋯	3.7
⋯	2017 Jul 8	$CS(5–4)$	244.93556	0.7	6.0×4.2	261	0.29	22.9
⋯	⋯	1.3 mm cont.	⋯	0.7	6.4×4.1	4984	⋯	4.3

Note. Here, ν_0 is the rest frequency of the spectral line, θ_P is the full width at half maximum (FWHM) size of the primary beam, $\theta_{maj} \times \theta_{min}$ is the FWHM size of the synthesized beam, ΔV_{BW} is the spectral bandwidth, and ΔV_{chan} is the spectral resolution.

Table 3
Archival Data

Survey	Telescope	Wavelength/ Energy	Spatial Resolution	Reference
GLIMPSE	*Spitzer*	3.6 μm	$<2''$	1, 2
GLIMPSE	*Spitzer*	8 μm	$<2''$	1, 2
MIPSGAL	*Spitzer*	24 μm	$6''$	3
MAGPIS	VLA	20 cm	$5\rlap{.}''4 \times 6\rlap{.}''2$	4
VGPS	VLA	21 cm	$1' \times 1'$	5
GRS	FCRAO 14 m	$^{13}CO(1–0)$ - 2.7 mm	$46''$	6
H.E.S.S. Survey of Inner Galaxy	H.E.S.S.	0.1–100 TeV	$\sim0\rlap{.}°1$	7

References. (1) Benjamin et al. (2003); (2) Churchwell et al. (2009); (3) Carey et al. (2009); (4) Helfand et al. (2006); (5) Stil et al. (2006); (6) Jackson et al. (2006); (7) Aharonian et al. (2006).

and we imaged the data using CASA's `clean` algorithm with Briggs weighting and the robustness parameter set to 0.5.

G23.33-0.30 was also recently observed by Killerby-Smith (2018) using the VLA in the A array configuration, which only detected $NH_3(3, 3)$ emission. The A array observation used the same calibrators as the D array, but the bandpass/flux calibrator was partially resolved by the A array's long baselines. Consequently, the fluxes measured from the A array data are lower limits. The spectral band for the A array observations was shifted to lower V_{LSR} compared to the D array, so the D array observations were able to detect emission up to $V_{LSR} = 90$ km s^{-1}, while the A array observations could only detect emission up to $V_{LSR} = 75$ km s^{-1}. The A array data were also reduced using CASA 5.1.1-5 and were imaged using CASA's `clean` algorithm with natural weighting.

2.2. ACA Observations

We observed G23.33-0.30 with the ACA using three pointings and five 50 minute execution blocks in two spectral setups. The first spectral setup was used to observe $SiO(5–4)$ and was executed four times, and the second spectral setup was used to observe $CS(5–4)$ and was executed once. For both spectral setups, we performed the bandpass calibration using observations of J1924-2914 and the phase calibration using periodic observations of J1743-0350. For the first spectral setup, we performed the flux calibration using observations of J1733-1304, and for the second spectral setup, we used observations of J1751+0939. The ACA data were calibrated by the ALMA data reduction pipeline and imaged using CASA 4.7.2. We carried out imaging using CASA's `tclean` algorithm with Briggs weighting and the robustness parameter set to 0.5.

2.3. SMA Observations

We observed G23.33-0.30 using the SMA for an eight-hour track in the compact configuration. We performed the bandpass calibration using observations of 3C454.3, the flux calibration using observations of Neptune, and the phase calibration using periodic observations of 1743-038. We calibrated the data using MIR,[11] an IDL-based data reduction software package, and converted the calibrated data to the MIRIAD[12] format for imaging using the `mir2miriad` procedure. We imaged the data with MIRIAD 4.3.8 using MIRIAD's `clean` algorithm with Briggs weighting and the robustness parameter set to 1.

3. Results

Figure 2 shows the 8 μm Galactic Legacy Infrared Midplane Survey Extraordinaire (GLIMPSE; Benjamin et al. 2003; Churchwell et al. 2009) image of G23.33-0.30, with the VLA $NH_3(2, 2)$ integrated intensity overlaid as contours. Clearly, the thermal $NH_3(2, 2)$ emission traces the IRDC filament, while a gap in the 8 μm extinction ($l = 23\rlap{.}°328$) corresponds to a gap in the $NH_3(2, 2)$ emission. The $\sim3''$ spatial resolution of the D array has resolved the bright, narrow $NH_3(3, 3)$ line at $V_{LSR} \sim 56$ km s^{-1} detected by HOPS and RAMPS into two point-like sources, while also revealing another potential maser at $V_{LSR} \sim 76$ km s^{-1}, $<10''$ away from the other two sources. The VLA A array observations of G23.33-0.30 (Killerby-Smith 2018)

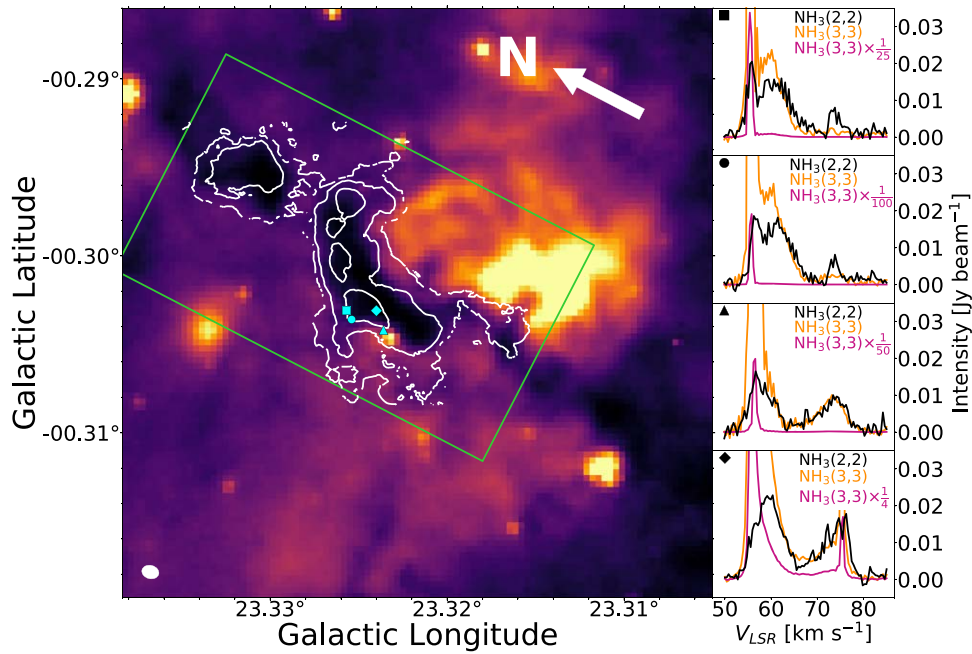[11] https://www.cfa.harvard.edu/rtdc/SMAdata/process/mir/
[12] https://www.atnf.csiro.au/computing/software/miriad/

Figure 2. Left: GLIMPSE 8 μm map of G23.33-0.30 with VLA $NH_3(2, 2)$ integrated intensity contours overlaid at 10, 50, and 150 mJy beam^{-1} km s^{-1}. The VLA D Array beam is shown in the lower left corner of the map, and the arrow in the upper right corner points to the north celestial pole. The green rectangle shows the region used to make the position–velocity diagram in Figure 6. The symbol markers indicate the positions of the $NH_3(3, 3)$ maser candidates. The thermal NH_3 emission traces an IRDC filament. Right: VLA D array $NH_3(2, 2)$ and (3, 3) spectra toward the four maser candidates, where the symbol markers in the upper left of each plot correspond to those in the GLIMPSE 8 μm map. The $NH_3(3, 3)$ spectra are presented both at their true amplitude and scaled for comparison.

resolved one of the maser candidates detected by the D array into two sources. The positions of the four maser candidates are shown with symbol markers in Figure 2, which also displays the $NH_3(2, 2)$ and $NH_3(3, 3)$ spectra toward each source. The spectra show that the suspected $NH_3(3, 3)$ maser emission is much narrower and brighter than the thermal $NH_3(2, 2)$ and (3, 3) emission. Three of the maser candidates have velocities near the peak of the narrowest $NH_3(2, 2)$ component at 56 km s^{-1}, while the faintest is found near a component peaking at 77 km s^{-1}.

Figure 3 illustrates the unusual kinematics in G23.33-0.30. The left panels show the $NH_3(2, 2)$, CS(5–4), and SiO(5–4) first-moment maps of the filament, with their respective integrated intensity contours overlaid, while the right panels show spectra taken across the width of the filament. The $NH_3(2, 2)$ and CS(5–4) data reveal a velocity discontinuity between a broad line component peaking at $V_{LSR} \sim 60$ km s^{-1} that is associated with the left edge of the filament and a narrower component at $V_{LSR} \sim 77$ km s^{-1} that is associated with the right side. The $NH_3(2, 2)$ data exhibit an additional narrow velocity component at $V_{LSR} \sim 56$ km s^{-1}, peaking near the velocities of three of the maser candidates. The SiO(5–4) emission is extremely broad and peaks primarily at $V_{LSR} < 76$ km s^{-1}. With the ACA's large spectral bandwidth, we are also able to detect emission near $V_{LSR} = 100$ km s^{-1}. We do not show this emission in any figures, because it is associated with two background sources unrelated to G23.33-0.30.

G23.33-0.30 exhibits bright emission from all of the observed NH_3 inversion transitions. Figure 4 displays the $NH_3(1, 1)$ through (6, 6) first-moment maps with integrated intensity contours overlaid. The linear features in the $NH_3(3, 3)$ map are a result of cleaning artifacts, not real emission. The emission from the higher-energy transitions ($NH_3(4, 4)$ through (6, 6)) is strongest at lower V_{LSR} and displays broad line

widths similar to those of the 60 km s^{-1} $NH_3(2, 2)$ velocity component. The highest-energy transition, $NH_3(6, 6)$, features particularly bright emission compared to $NH_3(5, 5)$, and even displays amplitude ratios of $NH_3(6, 6)/(4, 4) > 1$ near the peak of the $NH_3(6, 6)$ emission. In contrast to the $NH_3(1, 1)$ and (2, 2) data, the $NH_3(4, 4)$ through (6, 6) emission peaks only at $V_{LSR} \leqslant 76$ km s^{-1}, but exhibits a velocity discontinuity between components peaking at $V_{LSR} \sim 59$ and 75 km s^{-1}.

Figure 5 shows the SMA ^{13}CO(2–1), $C^{18}O$(2–1), 1.3 mm continuum, and ACA 1.3 mm continuum data. Due to the ACA's good uv coverage at shorter baselines, the continuum emission detected by the ACA traces the larger-scale filament, while the SMA continuum observations are primarily sensitive to the compact continuum cores. Three of the continuum cores, MM1, MM2, and MM3, lie along the filament. Because the bright mm core west of the filament is coincident with emission near $V_{LSR} = 100$ km s^{-1}, it is not associated with G23.33-0.30. The SMA ^{13}CO(2–1) and $C^{18}O$(2–1) emission peaks at $V_{LSR} \sim 77$ km s^{-1} between MM1 and MM2. The ^{13}CO(2–1) and $C^{18}O$(2–1) spectra peak at $V_{LSR} \sim 77$ km s^{-1} toward each of the cores associated with G23.33-0.30. There is also ^{13}CO(2–1) emission at lower V_{LSR} appearing mainly on the eastern edge of the filament in the range $V_{LSR} = 56–70$ km s^{-1}.

Figure 6 displays the $NH_3(2, 2)$ intensity integrated along lines of constant R.A. Because the filament points roughly north to south, the figure shows the variation of the gas kinematics along G23.33-0.30's length. We have also over-plotted the positions and velocities of the $NH_3(3, 3)$ maser candidates and the positions of the continuum sources MM1, MM2, and MM3. While the vast majority of the emission is at $V_{LSR} < 78$ km s^{-1} and displays broad line widths, a small portion of the filament between MM2 and MM3 exhibits narrow line emission peaking at $V_{LSR} \sim 78$ km s^{-1}. This
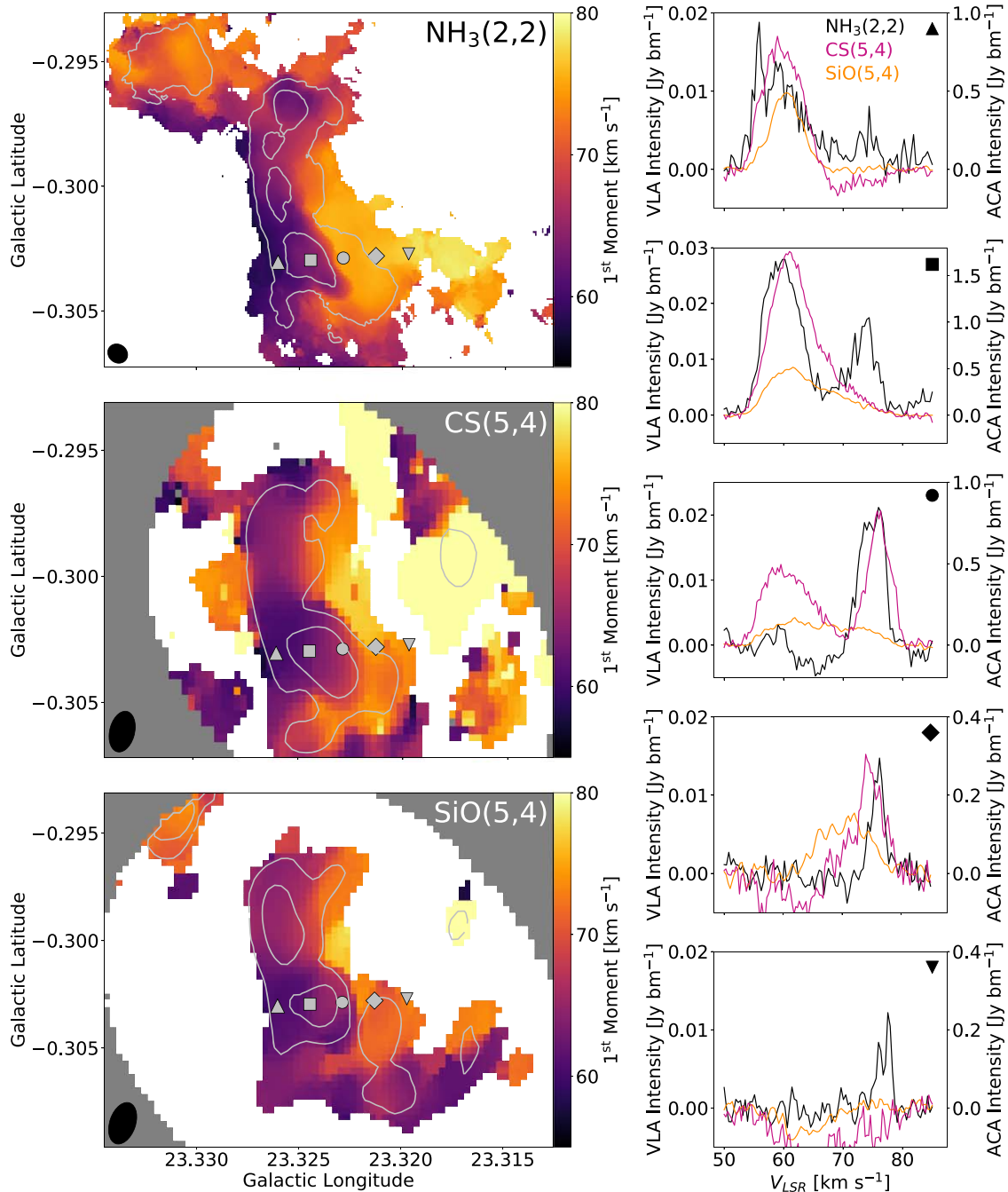
Figure 3. Left: NH$_3$(2, 2) (top), CS(5–4) (middle), and SiO(5–4) (bottom) first-moment maps overlaid with integrated intensity (moment 0) contours at 0.05 and 0.15, 2 and 8, and 1 and 4 Jy beam^{-1} km s^{-1}, respectively. The symbols overlaid correspond to the locations of the spectra to the right. Right: NH$_3$(2, 2) (black), CS(5–4) (magenta), and SiO(5–4) (orange) spectra from the positions indicated by the symbol markers in the left panels. The left axis corresponds to the NH$_3$(2, 2) spectra, while the right axis corresponds to the CS(5–4) and SiO(5–4) spectra. These data reveal a velocity discontinuity across the width of the filament.

narrow line emission corresponds to the southernmost section of the filament detected in NH$_3$(2, 2), but not SiO(5–4). The gas north of this narrow line emission is at lower V_{LSR} and composed of two components: a narrow component at $V_{\mathrm{LSR}} \sim 56$ km s^{-1} that is spatially and spectrally coincident with three of the NH$_3$(3, 3) maser candidates (Figure 2), and a turbulent component peaking at $V_{\mathrm{LSR}} = 60$–76 km s^{-1}. The section of the filament associated with the NH$_3$(3, 3) maser candidate at $V_{\mathrm{LSR}} = 76.4$ km s^{-1} is less turbulent and less blueshifted than the northern part of the filament. Figure 6 also reveals slight deficits in emission in the range $67 < V_{\mathrm{LSR}} < 75$ km s^{-1} at the positions of MM1 and MM2, while the

NH$_3$ emission toward MM3 reveals a velocity discontinuity between components peaking at $V_{\mathrm{LSR}} = 74$ km s^{-1} and $V_{\mathrm{LSR}} = 78$ km s^{-1}.

4. Analysis

4.1. NH$_3$(3, 3) Maser Emission

We determined the position and flux of each NH$_3$(3, 3) maser candidate by first fitting spectra to determine line amplitudes and then fitting these amplitude maps to estimate the positions. We used the Python Markov chain Monte Carlo (MCMC) fitting package `emcee` (Foreman-Mackey et al.
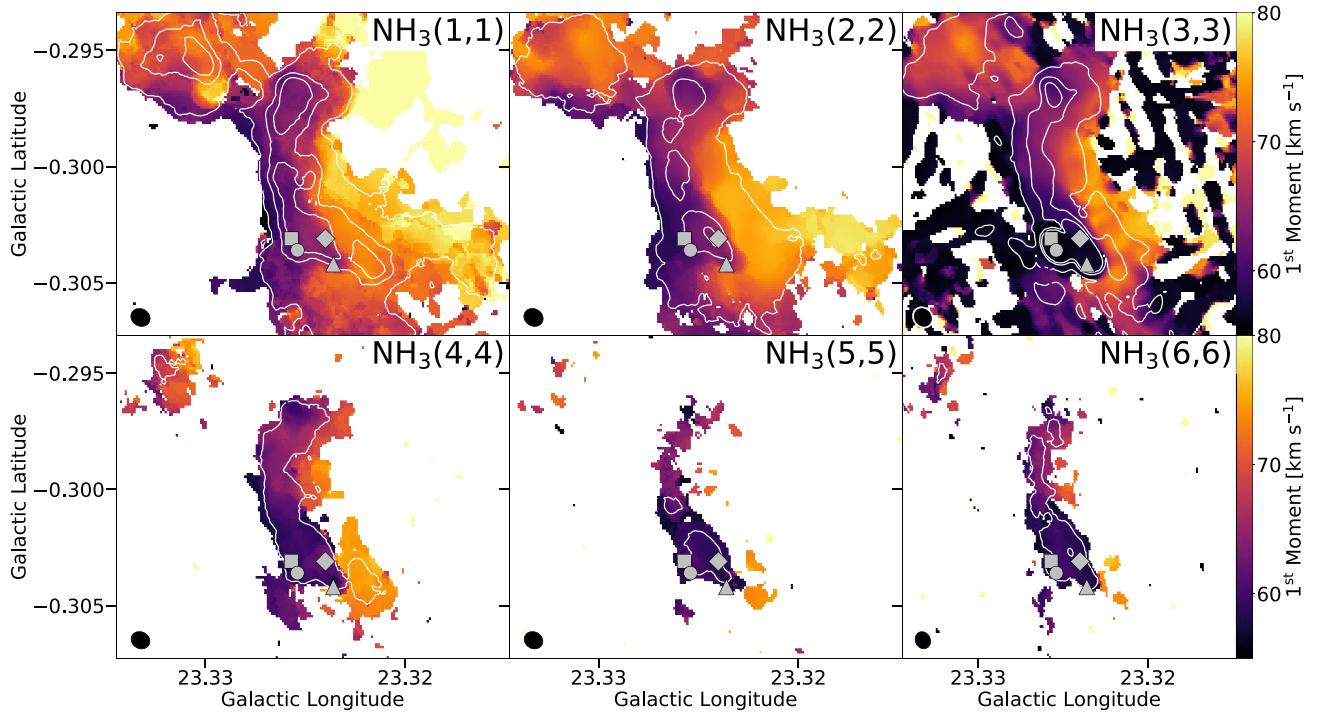
Figure 4. NH$_3$(1, 1) (top left), (2, 2) (top middle), (3, 3) (top right), (4, 4) (bottom left), (5, 5) (bottom middle), and (6, 6) (bottom right) first-moment maps overlaid with integrated intensity contours at 25, 150, and 250 mJy beam^{-1} km s^{-1}. The silver symbol markers indicate the positions of the NH$_3$(3, 3) masers and the synthesized beam for each transition is shown in the lower left of the map.

2013) to fit both the narrow line emission in the data cube and the resulting maps of the line amplitudes. We fit the narrow line emission with a Gaussian model and fit the amplitude maps with a model of the synthesized beam, as we expect maser emission to be unresolved. Table 4 presents the A array fit results for the sources peaking at 56–57 km s^{-1} and the D array fit results for the source peaking at 76 km s^{-1}, as well as the symbol markers corresponding to each source shown in Figures 2, 4–6. We display the best-fit values for each source's Galactic coordinate position (l, b), flux (I_ν), LSR velocity (V_{LSR}), velocity dispersion (σ), and line brightness temperature (ΔT_B).

Maser emission occurs in gas with a population inversion, with more molecules in the upper state of a transition than expected in local thermodynamic equilibrium (LTE). Population inversions in the NH$_3$(3, 3) transition are a result of collisions with H$_2$ molecules (Walmsley & Ungerechts 1983). The brightness temperature of a spectral line is given by $\Delta T_B = (T_{ex} - T_{bkg})(1 - e^{-\tau_\nu})$, where T_{ex} is the transition's excitation temperature, T_{bkg} is the background temperature, and τ_ν is the optical depth at frequency ν. If the molecular transition is in LTE with gas at temperature T_{gas} and the background radiation is dominated by the Cosmic Microwave Background (CMB), then $\Delta T_B \leqslant (T_{gas} - T_{CMB})$. On the other hand, a nonthermal population inversion produces negative values of τ_ν and T_{ex}, resulting in $\Delta T_B \gg T_{gas}$. Given the low temperatures expected in G23.33-0.30 ($T_{gas} \ll 10^4$ K), the three masers detected by the A array all exhibit $\Delta T_B \gg T_{gas}$, confirming their nonthermal nature. Because the source at $V_{LSR} = 76$ km s^{-1} was outside the velocity range of the A array data, the D array data provide our only measurement of its brightness temperature. This source is much fainter than the NH$_3$(3, 3) masers at $V_{LSR} \sim 56$–57 km s^{-1}, exhibiting a D array brightness temperature of only 17 K, which is comparable

to the temperatures typically measured in MCs. Although the D array brightness temperature cannot prove this source's nonthermal origin, it is approximately twice as bright as the peak thermal emission and exhibits a narrow line width similar to those of the confirmed masers. Moreover, the NH$_3$(3, 3) maser candidate has no corresponding velocity feature in any of the other NH$_3$ spectra. Consequently, we assume that the emission is nonthermal and will refer to this source as an NH$_3$(3, 3) maser. Thus, G23.33-0.30 hosts four NH$_3$(3, 3) masers: three associated with gas corresponding to the narrow NH$_3$(2, 2) velocity component near 57 km s^{-1}, and a fourth associated with the asymmetric line emission peaking at 77 km s^{-1}.

4.2. Thermal NH$_3$ Emission

In addition to accelerating gas, shocks can heat and add turbulence to the entrained gas component. Using the NH$_3$ modeling methods described by Hogge et al. (2018), we employed a PySpecKit (Ginsburg & Mirocha 2011) LTE NH$_3$ model to investigate whether the gas properties in G23.33-0.30 indicate a shock. We first derived NH$_3$ rotational temperatures (T_{rot}), velocity dispersions (σ), and LSR velocities (V_{LSR}) from the NH$_3$(1, 1) and (2, 2) data cubes. In order to exclude emission that would be too faint to provide accurate derived quantities, we only fit pixels that had NH$_3$(2, 2) integrated intensities greater than 10 mJy beam^{-1} km s^{-1}. Figure 7 displays maps of the best-fit parameter values for the velocity component with the larger NH$_3$(1, 1) through (2, 2) integrated intensity. The maps are overlaid with the positions of the NH$_3$(3, 3) masers, which we expect to reside at the locations of shock fronts. Although the presence of broad, overlapping, and asymmetric line shapes did not allow for accurate fit results over the full map, it is clear that the gas at higher V_{LSR} is generally colder and has a lower velocity dispersion than that at lower V_{LSR}. The southernmost section of
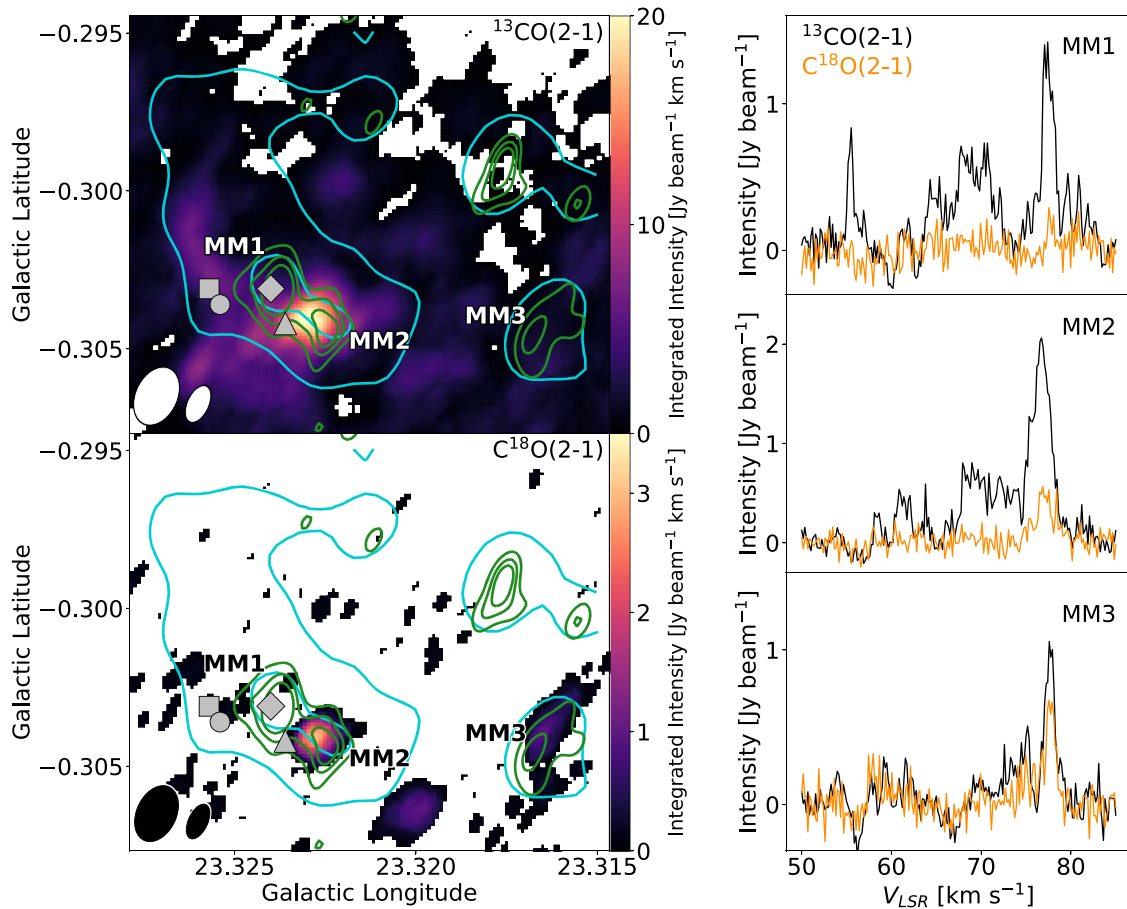
Figure 5. Left: color shows the SMA ^{13}CO (top) and C^{18}O (bottom) integrated intensity maps. Overlaid are 1.3 mm continuum contours from the ACA (cyan) at 4 and 30 mJy beam^{-1} and the SMA (green) at 3.5, 7, and 10.5 mJy beam^{-1}. The lowest contours correspond to a 5σ detection in both cases. The silver symbol markers indicate the positions of the masers. The continuum data reveal three compact cores associated with the filament: MM1, MM2, and MM3. Right: SMA ^{13}CO (black) and C^{18}O (orange) spectra toward MM1, MM2, and MM3. The brightest line in each spectrum peaks at $V_{LSR} \sim 77$ km s^{-1}.
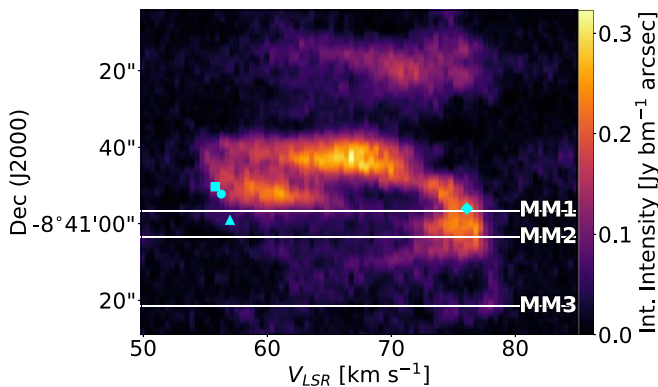
Figure 6. Plot of decl. vs. V_{LSR} made from the NH$_3$(2, 2) intensity integrated over the R.A. axis. The region over which we performed the integration is shown with a green box in Figure 2. Because G23.33-0.30 is oriented roughly north to south, this displays the gas kinematics along the filament's length. The cyan symbol markers indicate the positions and velocities of the NH$_3$(3, 3) masers and the white horizontal lines mark the positions of the molecular cores MM1, MM2, and MM3.

implied only moderate heating of the turbulent component ($\Delta T \sim 30$–40 K), the relatively bright emission from the higher-energy transitions NH$_3$(4–4) through (6, 6) indicates the presence of a hotter component to which the NH$_3$(1, 1) and (2, 2) amplitudes are insensitive. Consequently, we also performed fits using all of the observed para-NH$_3$ lines: NH$_3$(1, 1), (2, 2), (4, 4), and (5, 5). However, the best-fit models of the para-NH$_3$ lines often featured NH$_3$(1, 1) amplitudes that were smaller than those observed in the data and NH$_3$(2, 2) amplitudes larger than observed in the data. The fact that a single-temperature NH$_3$ model could not reproduce the para-NH$_3$ amplitudes suggests that there exist at least two temperature components. Thus, we performed fits using only NH$_3$(4, 4) and (5, 5) to better determine the temperature of the hotter component. The rotational temperatures based only on the NH$_3$(4, 4) and (5, 5) emission are $T_{rot}(4,4; 5,5) \sim 40$–200 K, much higher than those derived from NH$_3$(1, 1) and (2, 2). Thus, the shock has deposited significant thermal ($T_{preshock} \sim 10$–20 K versus $T_{preshock} \sim 40$–200 K) as well as turbulent ($\sigma_{preshock} < 1$ km s^{-1} versus $\sigma_{preshock} \sim 1$–5 km s^{-1}) energy into the filament.

4.3. Virial Analysis

We detected the 1.3 mm dust continuum emission from three compact sources associated with the filament, MM1, MM2, and MM3 (Figure 5), which represent molecular cores embedded within G23.33-0.30. We used an MCMC routine to fit the
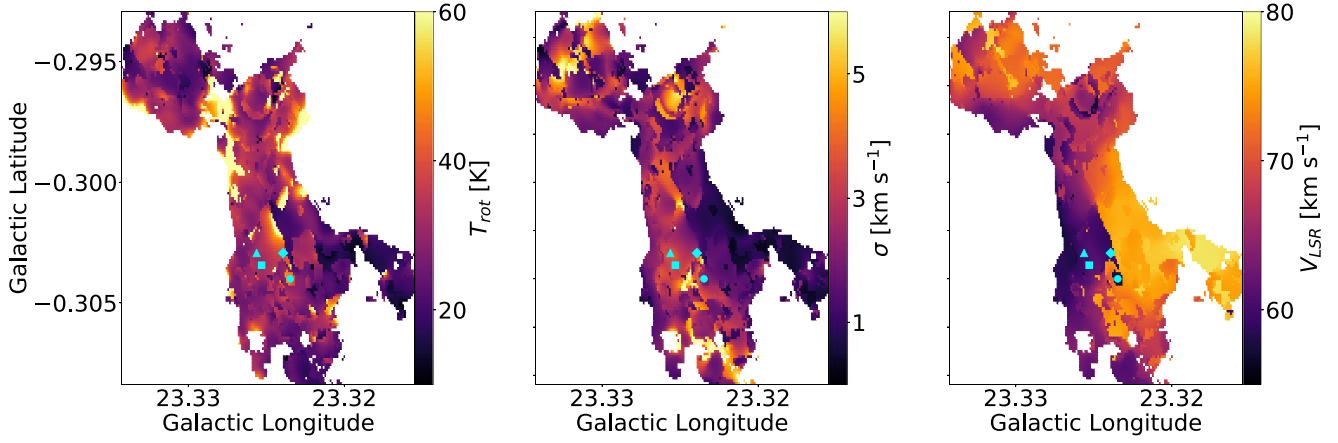
the filament, which has the largest measured V_{LSR}, was detected in NH$_3$(2, 2) but not SiO(5–4). It also corresponds to the region that is coldest and has the lowest velocity dispersion, likely indicating that the gas in this portion of the filament is unshocked and that $V_{LSR} \sim 78$ km s^{-1} is the filament's preshock LSR velocity. While our analysis of the NH$_3$(1, 1) and (2, 2) data

Figure 7. Maps of the NH$_3$ model best-fit values of $T_{\rm rot}$, σ, and $V_{\rm LSR}$, with the positions of the NH$_3$(3,3) masers overlaid. The gas at the preshock velocity is cold and has a low velocity dispersion, while the turbulent component is hot and has $\sigma > 1$ km s^{-1}.

Table 4
VLA NH$_3$(3, 3) Maser Properties

	Maser 1	Maser 2	Maser 3	Maser 4
Symbol	○	△	□	◇
Array	A	A	A	D
l (deg)	23.325713 ± 0.000001	23.325393 ± 0.000001	23.323564 ± 0.000001	23.323966 ± 0.000002
b (deg)	−0.303063±0.000001	−0.303566 ± 0.000001	−0.304137 ± 0.000001	−0.303085 ± 0.000002
I_ν (Jy)	1.312 ± 0.086	0.562 ± 0.049	0.453 ± 0.033	0.078 ± 0.001
$V_{\rm LSR}$ (km s^{-1})	56.319 ± 0.002	57.025 ± 0.007	55.754 ± 0.008	76.375 ± 0.003
σ (km s^{-1})	0.254 ± 0.003	0.242 ± 0.007	0.213 ± 0.005	0.187 ± 0.004
ΔT_B (K)	171300 ± 11230	73380 ± 6398	59150 ± 4309	16.7 ± 0.2

Table 5
Molecular Core Properties

	MM1	MM2	MM3
l (deg)	23.32384 ± 0.00002	23.32254 ± 0.00003	23.31680 ± 0.00003
b (deg)	−0.30314 ± 0.00001	−0.30459 ± 0.00002	−0.30465 ± 0.00002
R_1 (arcsec)	2.3 ± 0.1	2.3 ± 0.2	3.2 ± 0.3
R_2 (arcsec)	<1.1	<1.1	1.2 ± 0.1
R (pc)	<0.036	<0.035	0.044 ± 0.004
F_ν (mJy)	19.1 ± 0.2	13.9 ± 0.2	13.0 ± 0.3
M ($M_\odot$)	9.9 ± 4.7	7.2 ± 3.4	6.7 ± 3.2
$\sigma(^{13}{\rm CO})$ (km s^{-1})	0.57 ± 0.07	0.76 ± 0.02	0.43 ± 0.03
$\sigma({\rm C}^{18}{\rm O})$ (km s^{-1})	...	0.83 ± 0.09	0.46 ± 0.06
$M_{\rm vir}$ ($M_\odot$)	<36	<66	26 ± 3
α	<3.7	<9.2	3.9 ± 1.9

positions and sizes of the cores. The compact continuum emission from these cores is superposed on more extended emission. Consequently, we modeled the SMA continuum emission as the superposition of two elliptical Gaussians convolved with the SMA synthesized beam and estimated their positions (l, b) and sizes ($R_1 \times R_2$). This analysis implies that MM1 and MM2 are, at most, barely resolved by the SMA synthesized beam, so their best-fit sizes are upper limits. Table 5 displays the fit results.

The collapse of a molecular core depends on its turbulent energy content. Due to the added support against gravity, gas that is highly turbulent will have more difficulty collapsing to form stars than will gas with lower levels of turbulence. Thus, the line-of-sight velocity dispersion, along with the core

masses, can indicate whether the detected cores can collapse to form stars. In order to evaluate the fate of G23.33-0.30 and its associated molecule cores, we performed a virial analysis using the SMA continuum data and ^{13}CO(2–1) spectra. Neglecting magnetic fields and external pressure, the gravitational stability of a molecular core is dictated by the core mass ($M_{\rm core}$) and the virial mass ($M_{\rm vir}$) in the form of the virial parameter $\alpha = \frac{M_{\rm vir}}{M_{\rm core}}$, where $\alpha < 1$ indicates the potential for collapse. We determined $M_{\rm core}$ using the following equation from Hildebrand (1983)

$$M_{\rm core} = \mathbb{R} \frac{F_\nu D^2}{\kappa_\nu B_\nu(T)}, \qquad (1)$$

where $\mathbb{R}$ is the gas-to-dust mass ratio, F_ν is the source flux integrated within the FWHM boundary of the best-fit elliptical Gaussian, D is the distance to the source, κ_ν is the dust opacity, and $B_\nu(T_{\rm dust})$ is the Planck function at the dust temperature $T_{\rm dust}$. We assumed $\mathbb{R} = 100$ and $\kappa_{1.3\,\rm mm} = 0.9\ {\rm cm}^2\ {\rm g}^{-1}$, which is the opacity expected for dust with thin ice mantles at a number density of $10^6\ {\rm cm}^{-3}$ (Ossenkopf & Henning 1994). Because the values of $\mathbb{R}$ and $\kappa_{1.3\,\rm mm}$ are uncertain, we assume a 30% uncertainty on our assumed values. We adopted $D = 4.59^{+0.38}_{-0.33}$ kpc, the parallax distance to the high-mass star-forming region G23.01-0.41 that also resides within GMC 23.0-0.4 (Brunthaler et al. 2009). To estimate the dust temperature, we analyzed *Herschel* submm data (Molinari et al. 2010) using a single-temperature graybody model and the methods and assumptions described by Guzmán et al. (2015). We calculated dust temperatures in the range of $T_{\rm dust} \sim 16$–20 K and adopted $T_{\rm dust} = 18 \pm 2$ K, though the error may be larger because the dust temperature was derived from data at a larger angular scale ($\sim 35''$). We measured F_ν within the FWHM boundary of the best-fit models. Next, we determined $M_{\rm vir}$ using an equation given by MacLaren et al. (1988),

$$M_{\rm vir} = 3\left(\frac{5 - 2n}{3 - n}\right)\frac{R\sigma^2}{G}, \qquad (2)$$

where n specifies the density distribution ($\rho(r) \propto r^{-n}$), R is the radius of the core, σ is the line-of-sight velocity dispersion, and G is the gravitational constant. We assumed that $n = 1.8$, the average value for the radial density profile index found by Zhang et al. (2009) in IRDC cores. We estimated R from the geometric mean of the best-fit core radii $R = \sqrt{R_1 R_2}$ and measured σ from the SMA ^{13}CO(2–1) spectra toward the best-fit locations of the cores. We also detected C^{18}O(2–1) toward MM2 and MM3 and measured $\sigma(\rm C^{18}O) \approx \sigma(^{13}CO)$. Because the continuum data provide no kinematic information, the association between the continuum emission from a molecular core and a particular velocity component is sometimes ambiguous. Although we detected no obvious compact molecular line emission associated solely with the continuum cores, the SMA ^{13}CO emission peaking at $V_{\rm LSR} \sim 77\ {\rm km\ s}^{-1}$ suggests that the cores are associated with the preshock velocity component. Consequently, we have measured σ from the bright velocity component at $V_{\rm LSR} \sim 77\ {\rm km\ s}^{-1}$. We display the results of our virial analysis in Table 5. Although we have only determined upper limits on the virial parameter for MM1 and MM2, due to the unresolved core radii, the upper limit radii are similar to the expected size of prestellar molecular cores (Ward-Thompson et al. 1999), so the true virial parameters are unlikely to be much smaller than our upper limit estimates. Our analysis indicates that all of the cores embedded within G23.33-0.30 have $\alpha > 1$, implying that they are not currently unstable to collapse.

We also investigated the stability of the larger-scale filament by comparing G23.33-0.30's mass to the mass expected for a collapsing filament. We estimated G23.33-0.30's mass using *Herschel* submm data and the methods and assumptions described in Guzmán et al. (2015). We calculated a gas mass of $M \sim 600\ M_\odot$ for the $\sim 3 \times 0.2$ pc portion of G23.33-0.30 visible in Figure 2, which corresponds to a linear mass density

of $M/l \sim 200\ M_\odot\ {\rm pc}^{-1}$. For a typical dense molecular clump (pc size scale), the minimum mass required to form an 8 $M_\odot$ star is $\sim 260\ M_\odot$ (Sanhueza et al. 2017), assuming a star formation efficiency of 30% and a Kroupa (2001) initial mass function. Although this places G23.33-0.30 in the category of potentially high-mass star-forming filaments, the filament's highly blueshifted and turbulent gas make this less certain. The critical linear mass density above which a molecular filament is unstable to collapse is given by $(M/l)_{\rm crit} = 84(\Delta V)^2 M_\odot\ {\rm pc}^{-1}$ (Jackson et al. 2010), where ΔV is the FWHM line width. Although the velocity dispersion varies throughout G23.33-0.30, a typical value is $\sigma \sim 2\ {\rm km\ s}^{-1}$, which corresponds to $\Delta V \sim 5\ {\rm km\ s}^{-1}$. This value provides a critical linear mass density of $(M/l)_{\rm crit} \sim 2000\ M_\odot\ {\rm pc}^{-1}$, much larger than our estimate of G23.33-0.30's linear mass density. Thus, like G23.33-0.30's embedded cores, the filament is not massive enough to collapse, given the turbulent gas.

5. Discussion

5.1. Evidence of a Large-scale Shock

Although NH$_3$(3, 3) maser emission typically indicates shocked gas, the positions and velocities of the masers alone cannot distinguish between the protostellar outflow and SNR– MC interaction scenarios. On the other hand, the sharp velocity discontinuity across the width of the filament, which corresponds to an increase in temperature and velocity dispersion, implies a large-scale shock and greatly favors an SNR–MC interaction scenario. Moreover, the SiO(5–4) emission, which traces shocked gas (Caselli et al. 1997), is extended throughout the filament (Figure 3). While shocks from protostellar outflows could be consistent with the NH$_3$(3, 3) maser emission, the resulting SiO emission would be confined to narrow outflow jets emanating from the continuum cores. Because protostellar outflows cannot account for such extended SiO emission, it is more likely that a large-scale shock from an SNR is responsible.

Figure 8 shows plots of $T_{\rm rot}(1,1; 2,2)$ and $\sigma(1,1; 2,2)$ versus $V_{\rm LSR}$, as well as $T_{\rm rot}(4,4; 5,5)$ and $\sigma(4,4; 5,5)$ versus $V_{\rm LSR}$. The NH$_3$(4, 4) and (5, 5) emission is clearly more sensitive to the hot gas component than the NH$_3$(1, 1) and (2, 2) emission. The plots of $T_{\rm rot}(1,1; 2,2)$ and $\sigma(1,1; 2,2)$ versus $V_{\rm LSR}$ show that the gas at the preshock velocity ($V_{\rm LSR} = 77$–78 km s^{-1}) is generally colder and has a lower velocity dispersion than the turbulent component at lower $V_{\rm LSR}$, but the correlations among the parameters are not particularly tight. On the other hand, $T_{\rm rot}(4,4; 5,5)$ and $\sigma(4,4; 5,5)$, which are sensitive to the shocked component, exhibit a more coherent relationship with $V_{\rm LSR}$. The emission at $V_{\rm LSR} < 60$ km s^{-1} displays positive correlations among $T_{\rm rot}(4,4; 5,5)$, $\sigma(4,4; 5,5)$, and $V_{\rm LSR}$, while the emission at $V_{\rm LSR} > 60$ km s^{-1} displays negative correlations among these parameters. We speculate that these trends are a signature of the impact that triggered the NH$_3$(3, 3) maser emission.

In G23.33-0.30's reference frame ($V_{\rm LSR} \sim 77$ km s^{-1}), the gas component associated with the NH$_3$(3, 3) masers at $V_{\rm LSR} \sim 56$ km s^{-1} approaches the filament with a relative velocity of at least 20 km s^{-1}. The impacting gas component forms a shock and excites maser emission as it interacts with the filament. The impulse of the shock accelerates the filament gas, blueshifting it to lower $V_{\rm LSR}$, as well as increasing its temperature and velocity dispersion. This shock acceleration of
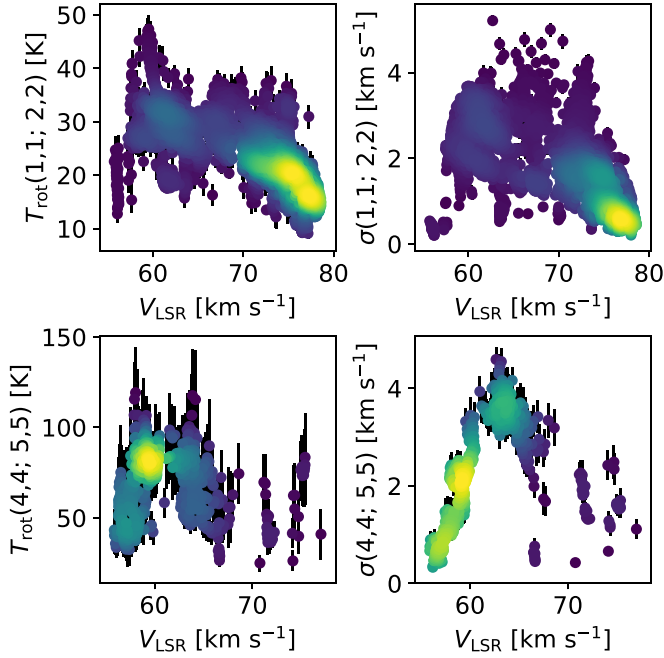
Figure 8. Plots of the NH$_3$ model best-fit values of $T_{\rm rot}$ and σ versus $V_{\rm LSR}$, where the symbol color corresponds to the density of points. Upper plots display the parameter values derived from the NH$_3$(1, 1) and (2, 2) spectra, while the lower plots show the values derived from the NH$_3$(4, 4) and (5, 5) spectra. We show only the fit results that have parameter errors below the 75th percentile and parameter values that are not pegged to their maximum nor their minimum values.

the filament gas accounts for the negative correlations among $T_{\rm rot}(4,4; 5,5)$, $\sigma(4,4; 5,5)$, and $V_{\rm LSR}$ for $V_{\rm LSR} > 60$ km s^{-1}. Simultaneously, the impacting gas component is decelerated by the interaction with the filament, due to G23.33-0.30's inertia. In the reference frame of the component at $V_{\rm LSR} \sim 56$ km s^{-1}, it encounters the dense filament approaching quickly and is impacted, redshifting it to higher $V_{\rm LSR}$, as well as increasing its temperature and velocity dispersion. This deceleration of the impacting component due to G23.33-0.30's inertia accounts for the positive correlations among $T_{\rm rot}(4,4; 5,5)$, $\sigma(4,4; 5,5)$, and $V_{\rm LSR}$ for $V_{\rm LSR} < 60$ km s^{-1}. Consequently, the hot, highly turbulent component at $V_{\rm LSR} = 60$–68 km s^{-1} likely represents the turbulent wake of the shock (Pittard & Parkin 2016).

Assuming the maser at $V_{\rm LSR} = 76.4$ km s^{-1} represents genuine nonthermal emission, it likely signals another shock front within the filament. This source is associated with gas at higher $V_{\rm LSR}$ and is much fainter than the other NH$_3$(3, 3) masers. Figure 6 suggests that the maser, MM1, and MM2 are all associated with a section of the filament that exhibits values of $T_{\rm rot}$, σ, and $V_{\rm LSR}$ that are intermediate between the turbulent component and the preshock component. Given that this portion of the filament is situated between a highly shocked region and an unshocked region of the filament, we speculate that it is at an earlier stage of shock interaction than the hot, turbulent component. The moderate temperature of this intermediately shocked component may in part explain the faintness of the maser at $V_{\rm LSR} = 76.4$ km s^{-1}. Figure 9 shows a non-LTE RADEX (van der Tak et al. 2007) plot of the expected NH$_3$(3, 3) optical depth ($\tau_{(3,3)}$) and brightness temperature ($\Delta T_B(3, 3)$) as a function of the gas kinetic temperature (T_k) and number density (n) for the derived beam-averaged column density ($N_{\rm NH_3} = 10^{15.5}$ cm^{-2}) and velocity dispersion ($\sigma = 1.7$ km s^{-1}) of the intermediately shocked

component. Large brightness temperatures and negative optical depths, which indicate strong masing, are only achieved for larger temperatures. At low temperatures, the RADEX model predicts that the gas should be either weakly masing or nonmasing. Given the low rotational temperature of the intermediately shocked component ($T_{\rm rot}(1,1; 2,2) \sim$ 20–25 K), the lower $\Delta T_B(3, 3)$ of the maser is expected. If the shock continues to heat this section of the filament, it is possible that the maser's brightness temperature will increase.

The large rotational temperatures of the hot, turbulent component demonstrate that the shock has heated the gas in the filament, but the NH$_3$(4, 4) and (6, 6) data also provide evidence of dust heating. NH$_3$ modeling by Faure et al. (2013) suggests that ortho-NH$_3$ ($K = 3n$) forms preferentially over para-NH$_3$ ($K \neq 3n$) on the surfaces of cold ($T < 30$ K) dust grains. In addition, the ortho-NH$_3$ ground state is at a lower energy than the para-NH$_3$ ground state, resulting in a larger amount of energy being needed to desorb para-NH$_3$ than ortho-NH$_3$ (Umemoto et al. 1999). Consequently, shocks that heat the icy mantles of cold dust grains release ortho-enhanced NH$_3$ into the gas phase and result in an ortho-to-para abundance ratio (OPR) larger than the statistical equilibrium value of OPR $=1$. Enhanced OPRs have previously been observed by Umemoto et al. (1999) in the L1157 outflow and by de Wilt et al. (2017) toward SNR–MC interactions. To confirm the presence of ortho-enhanced gas associated with G23.33-0.30, we fit the NH$_3$(4, 4) through (6, 6) spectra toward the peak of the NH$_3$(6, 6) emission. We calculated brightness temperature ratios of $\frac{\Delta T_B(5,5)}{\Delta T_B(4,4)} = 0.57 \pm 0.03$, $\frac{\Delta T_B(6,6)}{\Delta T_B(5,5)} = 2.71 \pm 0.13$, and $\frac{\Delta T_B(6,6)}{\Delta T_B(4,4)} = 1.54 \pm 0.06$. Figure 10 shows the NH$_3$(4, 4) through (6, 6) brightness temperature ratios predicted by RADEX for a range of temperatures and densities, assuming the column density ($N = 10^{15.5}$ cm^{-2}) and velocity dispersion ($\sigma = 1.75$ km s^{-1}) measured from the NH$_3$(4, 4) and (5, 5) spectra and OPR=1. The temperatures and densities corresponding to our measured value of $\frac{\Delta T_B(5,5)}{\Delta T_B(4,4)}$ are indicated by the white lines overlaid on each plot. If the turbulent gas component had OPR = 1, the lines would intersect our measured values of $\frac{\Delta T_B(6,6)}{\Delta T_B(5,5)}$ and $\frac{\Delta T_B(6,6)}{\Delta T_B(4,4)}$. However, our measured values for $\frac{\Delta T_B(6,6)}{\Delta T_B(5,5)}$ and $\frac{\Delta T_B(6,6)}{\Delta T_B(4,4)}$ are larger than any of the values on either plot, suggesting that OPR > 1 for the turbulent gas component. Although masing in the NH$_3$(6, 6) transition offers another possible explanation for the large ortho-to-para brightness ratios, the large velocity dispersion of the NH$_3$(6, 6) line ($\sigma \sim 1.5$ km s^{-1}) make this unlikely. Thus, G23.33-0.30 is associated with ortho-enhanced gas, implying that the shock has heated the filament's cold dust and sublimated NH$_3$ from their icy mantles.

5.2. W41's SNR–MC Interaction with GMC G23.0-0.4

Although MCs can experience shocks due to protostellar jets or H II regions, supernova shocks deliver a stronger impulse over a much shorter time span. Supernovae release roughly 10^{51} erg of energy near-instantaneously, sending powerful shock waves over tens of parsecs. Despite the fact that only $\sim$5–10% of the total energy is converted into kinetic energy in the shock (Walch & Naab 2015), the energy in a supernova shock can be sufficient to disrupt and disperse MCs and cores. Using a simple $E_{\rm shock} = \frac{1}{2}M_{\rm shocked}\Delta V^2$ energy transfer analysis, the mass displaced by an SNR shock is approximately given by $M_{\rm shocked} \sim \frac{2\Omega f_{\rm kin}E_{\rm SN}}{4\pi\Delta V^2}$, where Ω is the MC's solid angle
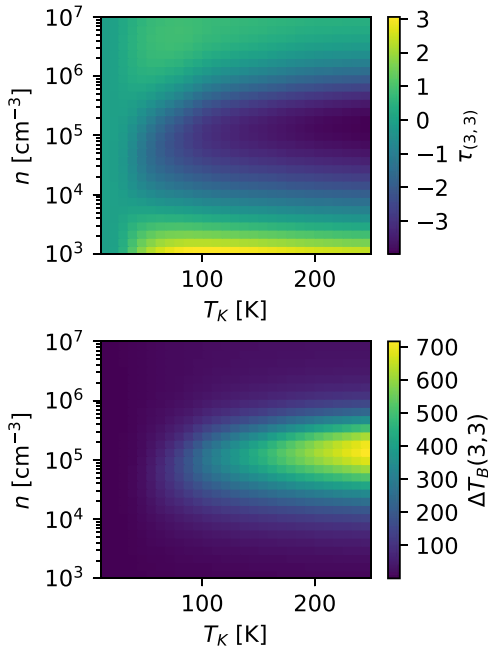
Figure 9. Plot of the RADEX NH$_3$(3, 3) optical depth ($\tau_{(3, 3)}$) (top) and brightness temperature (ΔT_B(3, 3)) (bottom) as a function of the kinetic temperature (T_k) and number density (n) for a column density of $N = 10^{15.5}$ cm^{-2} and a velocity dispersion of $\sigma = 1.7$ km s^{-1}.

at its distance from the supernova, $f_{\rm kin}$ is the kinetic efficiency of the SNR shock, $E_{\rm SN}$ is the total energy of the supernova, and ΔV^2 is the change in velocity of the shocked gas. Assuming that $E_{\rm SN} = 10^{51}$ erg, $f_{\rm kin} = 5\%$, $\Delta V = 10$ km s^{-1}, and Ω is the solid angle of a spherical cloud with a radius of 0.5 pc radius at 5, 10, or 20 pc away from the supernova, the gas mass displaced by the shock is 130, 35, or 9 $M_\odot$, respectively.

Given the uncertainty in the shock properties, the mass in the shocked portion of G23.33-0.30 is comparable to the mass able to be displaced by an SNR shock, implying that an SNR is a plausible source for the shock that is accelerating the molecular filament gas. Considering the suggestions of an SNR–MC interaction between SNR W41 and GMC G23.0-0.4 (Frail et al. 2013), W41 is an attractive progenitor for the large-scale shock impacting G23.33-0.30. An SNR shock would likely supply enough energy to explain G23.33-0.30's highly blueshifted emission, broad turbulent line widths, and increased temperature and velocity dispersion. Thus, we speculate that the turbulent, blueshifted gas observed in G23.33-0.30 is the result of a large-scale shock originating from the nearby SNR W41.

Figure 11 shows the Multi-Array Galactic Plane Imaging Survey (MAGPIS; Helfand et al. 2006) 20 cm continuum emission from W41 in color and the VLA Galactic Plane Survey (VGPS; Stil et al. 2006) 21 cm data as contours. W41 is an asymmetric shell-type supernova (Green 1991; Kassim 1992) suspected of interacting with the nearby GMC G23.0-0.4 at $V_{\rm LSR} = 77$ km s^{-1} (Su et al. 2015). Frail et al. (2013) detected two 1720 MHz OH maser candidates, known to trace SNR–MC interactions (Wardle & Yusef-Zadeh 2002), coincident with W41's central continuum peak. W41 is also coincident with HESS J1834-087 (Aharonian et al. 2006; Albert et al. 2006), a source of TeV emission thought to be triggered by W41's interaction with a GMC (Tian et al. 2007). Deep follow-up observations with H.E.S.S. revealed that the TeV emission is composed of a point-like source and an
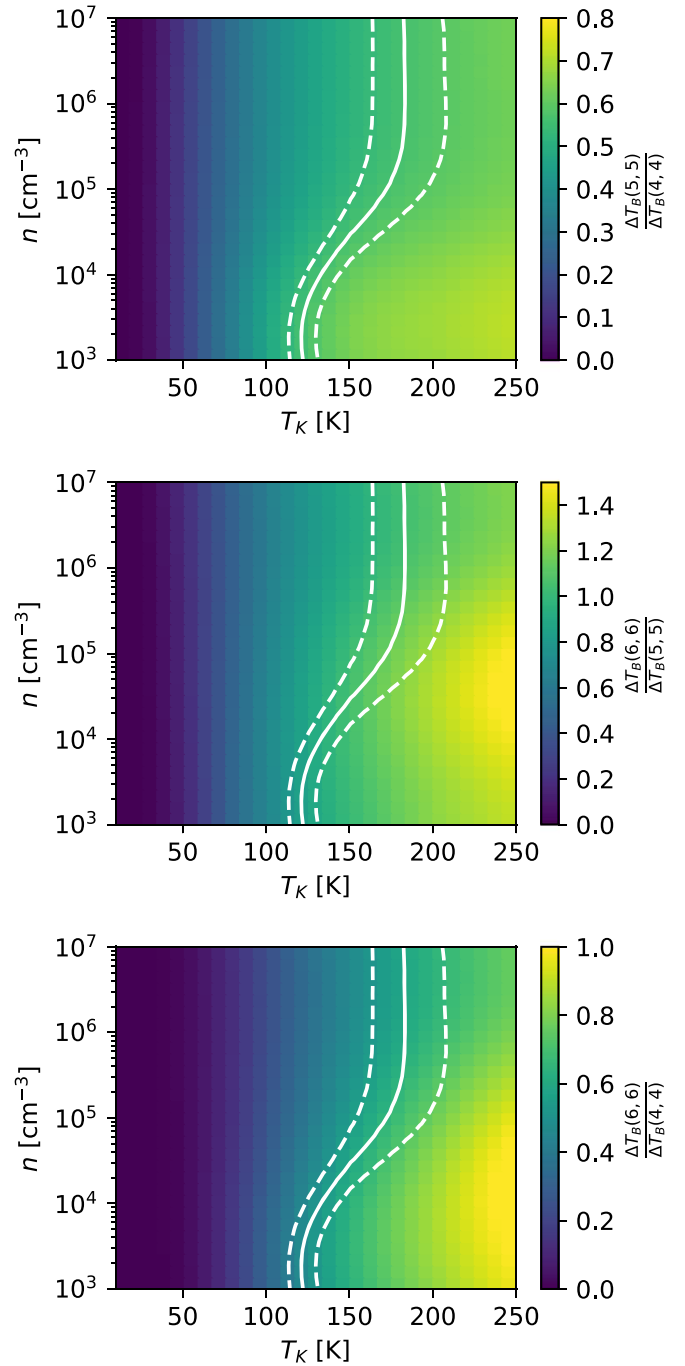

Figure 10. Plot of RADEX brightness temperature ratios as a function of the kinetic temperature (T_k) and number density (n): $\frac{\Delta T_B(5,5)}{\Delta T_B(4,4)}$ (top), $\frac{\Delta T_B(6,6)}{\Delta T_B(5,5)}$ (middle), and $\frac{\Delta T_B(6,6)}{\Delta T_B(4,4)}$ (bottom). We assume a column density of $N = 10^{15.5}$ cm^{-2} and a velocity dispersion of $\sigma = 1.75$ km s^{-1}. The solid white line in each plot marks the temperatures and densities corresponding to the $\frac{\Delta T_B(5,5)}{\Delta T_B(4,4)} = 0.570 \pm 0.026$ measured toward the peak of the NH$_3$(6, 6) emission. The dashed lines mark the 1σ uncertainties on the measured amplitude ratio.

extended component (H. E. S. S. Collaboration et al. 2015). Although the pulsar candidate CXOU J183434.9-08444 (Misanovic et al. 2011) may account for the point-like component of the TeV emission, H. E. S. S. Collaboration et al. (2015) argued that the extended TeV emission is best explained by the SNR–MC interaction.
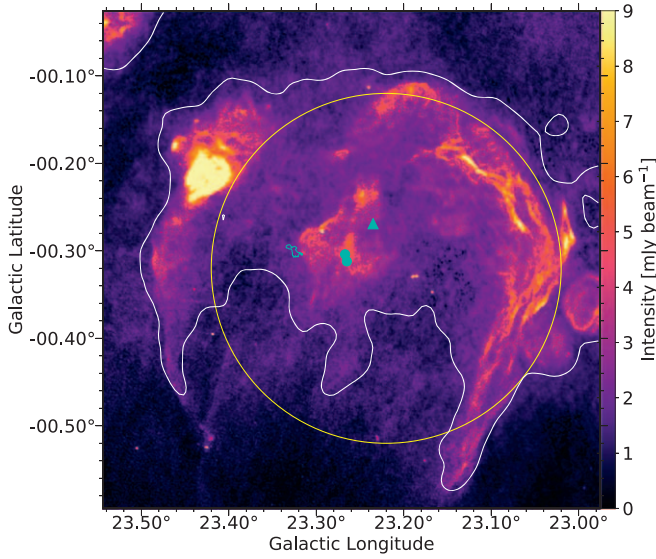
Figure 11. Color shows the MAGPIS 20 cm continuum data. The white contours show the VGPS 21 cm continuum data at 30 K and the cyan contours show the VLA NH$_3$(2, 2) integrated intensity data from G23.33-0.30 at 50 mJy beam^{-1} km s^{-1}. The cyan circles coincident with the central 20 cm continuum peak indicate the positions of two 1720 MHz OH maser candidates, which have velocities near 75 km s^{-1}, and the cyan triangle shows the position of the pulsar candidate CXOU J183434.9-08444. The large yellow circle displays the fitted position and FWHM size of the extended component of HESS J1834-087's TeV γ-ray emission.

Figure 12. Color shows the MIPSGAL 24 μm (red), GLIMPSE 8 μm (green), and 3.6 μm (blue) MIR data. For reference, we show the MAGPIS 20 cm continuum data with contours at 3 mJy beam^{-1}, as well as the data overlaid in Figure 11.

The MIR emission toward the W41 region from GLIMPSE and the MIPS Galactic Plane Survey (MIPSGAL; Carey et al. 2009) is shown in Figure 12, displaying a rich and complicated star-forming complex. These data reveal filamentary IRDCs and several sources of bright MIR emission, but provide no kinematic information about the molecular gas near W41. In order to better understand the kinematics of the molecular gas in the W41 region, we analyzed the Galactic Ring Survey (GRS; Jackson et al. 2006) ^{13}CO(1–0) data. The VLA NH$_3$ data revealed three prominent velocity components: a narrow component at $V_{\rm LSR} \sim 56$ km s^{-1} that appears to be associated with three of the NH$_3$(3, 3) masers, a broad, turbulent component at $V_{\rm LSR} \sim 60$ km s^{-1}, and a relatively asymmetric line peaked at $V_{\rm LSR} \sim 77$ km s^{-1}, which is associated with the NH$_3$(3, 3) maser at $V_{\rm LSR} \sim 76$ km s^{-1}. We inspected the ^{13}CO data for emission associated with these velocity components and created maps of the integrated intensity in 2 km s^{-1} windows centered on these velocities. We also found another distinct ^{13}CO(1–0) velocity component peaking at 81–82 km s^{-1}, which is spatially and spectrally adjacent to the other emission. Figure 13 shows the GRS ^{13}CO(1–0) data integrated in the velocity ranges indicated in each panel, with the MAGPIS continuum overlaid for comparison. The lower-velocity emission centered at 56 and 60 km s^{-1} displays emission near the positions of W41's central 20 cm continuum peak and G23.33-0.30. On the other hand, the emission at 77 km s^{-1} clearly traces GMC G23.0-0.4, but exhibits a conspicuous deficit in emission where W41's central continuum emission peaks. Finally, the 82 km s^{-1} component traces an MC, seen as a collection of IRDC filaments in Figure 12, that could represent a nearby background cloud or some other component of the GMC. Tian et al. (2007) also noted the association between the lower-velocity emission, W41's continuum, and HESS J1834-087, but they assumed that the emission represented a separate GMC with which W41 was
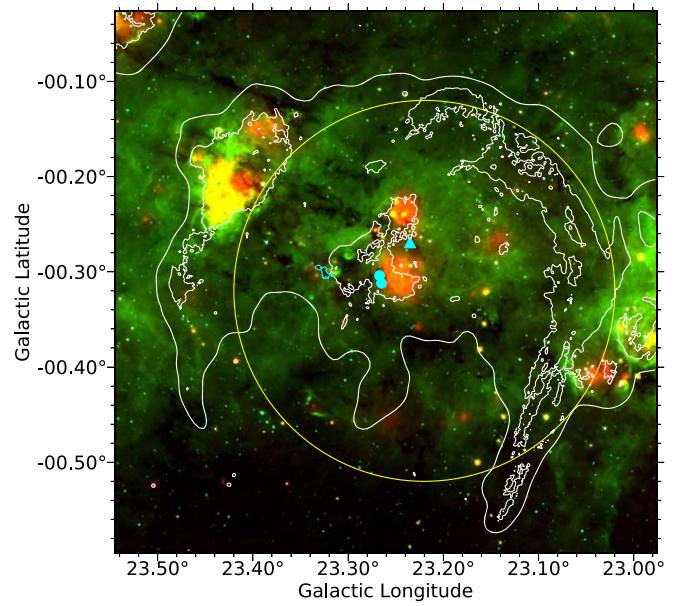
interacting. If this were true, the emission from GMC G23.0-0.4 would likely be uncorrelated with the central 20 cm continuum peak, rather than anticorrelated. Moreover, Figure 14 shows that the lower-velocity emission at 56 and 60 km s^{-1} and the GMC emission at 77 km s^{-1} also appear to be anticorrelated. In light of the agreement between the velocities of the 1720 MHz OH maser candidates and the GMC, as well as the apparent anticorrelation between the lower-velocity emission and the GMC emission, we argue that these lower-velocity components are associated with GMC G23.0-0.4 and the SNR–MC interaction.

Frail et al. (2013) also detected an OH absorption feature at 76 km s^{-1}, which places W41 within or behind G23.0-0.4. In addition, Leahy & Tian (2008) measured a maximum H I absorption velocity of 78 ± 2 km s^{-1} toward W41, indicating that W41's progenitor may have formed within G23.0-0.4. The Reid et al. (2014) near-kinematic distance for $V_{\rm LSR} = 77$ km s^{-1} toward G23.33-0.30 is $4.41^{+0.27}_{-0.26}$ kpc and the maser parallax distance to the nearby HMSFR G23.01-0.41 is $4.59^{+0.38}_{-0.33}$ kpc (Brunthaler et al. 2009). Considering that the GRS ^{13}CO(1–0) data strongly imply that G23.01-0.41 and G23.33-0.30 both reside within GMC G23.0-0.4, we adopt the maser parallax distance for W41. W41's angular size of $\sim0°.5$ implies that the SNR has a physical diameter of $\sim$40 pc. This size is in agreement with estimates from the Sedov relation (Sedov 1959), assuming a reasonable average density (~6 cm^{-3}) and SNR age ($\sim2 \times 10^5$ yr) (Tian et al. 2007).

Given that these data are consistent with an interaction between SNR W41 and GMC G23.0-0.4, we further speculate that the ^{13}CO(1–0) emission with $V_{\rm LSR} = 60$–75 km s^{-1} (not shown) in the vicinity of the W41's central 20 cm continuum peak represents gas from G23.0-0.4 that has been shock-accelerated to its current velocity. The $V_{\rm LSR} = 56$ km^{-1} component seems to correspond to the component associated with the NH$_3$(3, 3) masers in G23.33-0.30. This velocity component, which presumably represents gas moving with the
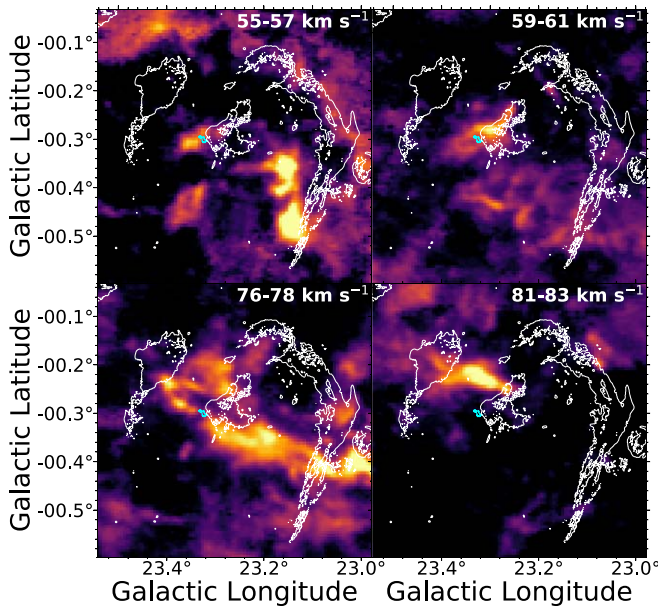
Figure 13. Color shows the GRS ^{13}CO(1–0) integrated intensity over the ranges specified in each panel. We show the MAGPIS 20 cm continuum data with contours at 3 mJy beam^{-1} for reference. The cyan contours show the VLA NH$_3$(2, 2) integrated intensity data from G23.33-0.30 at 50 mJy beam^{-1} km s^{-1}.
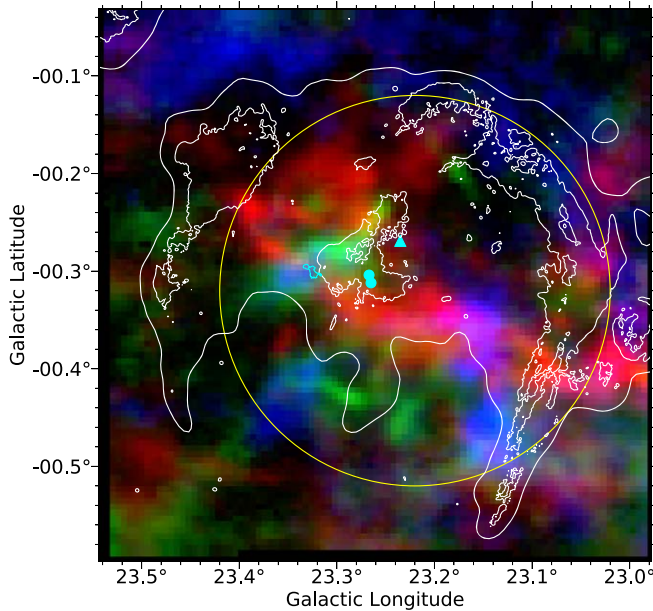

Figure 15. Color shows the MIPSGAL 24 μm (red), GLIMPSE 8 μm (green), and 3.6 μm (blue) MIR data. MAGPIS 20 cm continuum data are shown with white contours at 3 mJy beam^{-1}, and magenta contours show the VLA NH$_3$(2, 2) integrated intensity data of G23.33-0.30 at 50 mJy beam^{-1} km s^{-1}. Circles show the nearby sources from the *WISE* H II Region Catalog. Red circles indicate known H II regions with RRL detections, cyan circles indicate candidate H II regions that exhibit continue emission but lack RRL detections, and yellow circles indicate radio-quiet candidate H II regions, which exhibit the MIR characteristics of an H II region but lack radio continue emission and RRL emission.

Figure 14. Color shows the GRS ^{13}CO integrated intensity over the range 55–57 km s^{-1} (blue), 59–61 km s^{-1} (green), and 76–78 km s^{-1} (red). Symbols and contours as in Figure 12.

largest velocity relative to G23.33-0.30, appears to be streaming past and interacting with the filament. The existence of unshocked gas within G23.33-0.30, as well as ^{13}CO(1–0) emission at the preshock velocity adjacent to the filament, imply that the interaction between SNR W41 and G23.33-0.30 is ongoing. This agrees with our interpretation of the interferometric data, which exhibit emission at $V_{\mathrm{LSR}} = 77$–78 km s^{-1} (preshock gas), $V_{\mathrm{LSR}} = 60$–75 km s^{-1} (turbulent shock wake), and $V_{\mathrm{LSR}} = 56$–57 km s^{-1} (gas entrained in shock front). A caveat to this interpretation is that W41 lies near the plane of the Galaxy, so the line of sight
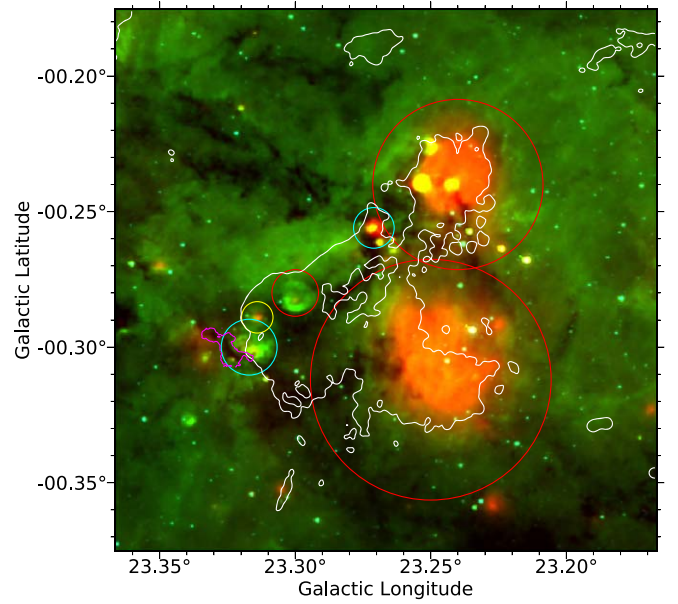
toward the SNR is crowded with MCs at various velocities, which could confuse our interpretation. In addition, feedback from previous generations of high-mass stars can accelerate gas and create molecular gas structures that are physically close, but have different V_{LSR}. Thus, it is possible that the molecular gas with $V_{\mathrm{LSR}} = 60$–75 km s^{-1} is not currently associated with the GMC, but is in fact a remnant of the larger GMC structure that is being impacted by the SNR shock from W41. On the other hand, it is difficult to imagine such a scenario producing the striking anticorrelation between the GMC velocity component and the $V_{\mathrm{LSR}} = 60$ km s^{-1} velocity component. Although more observations are needed to determine the true relationship between these velocity components, an SNR–MC interaction seems to best explain the large turbulent line widths, heating, NH$_3$(3, 3) masers, and blueshifted emission observed in G23.33-0.30.

An alternative explanation for G23.33-0.30's large turbulent line widths is energy added by nearby H II regions. Figure 15 shows a zoomed view of the MIR emission toward W41's central continuum peak. The overlaid circles show the positions and sizes of several nearby H II regions and candidate H II regions from the *WISE* Catalog of Galactic H II regions (Anderson et al. 2014). While it is clear that these H II regions cannot account for all of the 20 cm continuum emission toward W41's center, it is likely that they contribute a portion of the emission. The red circles indicate H II regions that have known velocities from radio recombination lines (RRLs): G023.250-00.240 ($V_{\mathrm{LSR}} = 76.3$ km s^{-1}), G023.265-00.301a ($V_{\mathrm{LSR}} = 73.1$ km s^{-1}), and G023.295-00.280 ($V_{\mathrm{LSR}} = 61.6$ km s^{-1}). Although these velocities may indicate an association with the GMC or the 60 km s^{-1} ^{13}CO(1–0) component, it is unlikely that these sources could account for the significant energy input implied by G23.33-0.30's large turbulent line widths,

given their angular separation from G23.33-0.30. The source with the smallest angular separation from G23.33-0.30, the candidate H II region G023.317-0.300, lacks a reliable velocity from an RRL detection, but its position behind G23.33-0.30 makes it an attractive alternative source for G23.33-0.30's turbulence. On the other hand, our interferometric data exhibit broad SiO(5–4) and CS(5–4) line emission peaking at $V_{LSR} = 97 \, \mathrm{km \, s^{-1}}$ near the center of the candidate H II region, potentially signifying its association with the background source HMSFR G23.44-0.18, which has a maser parallax distance of $5.88^{+1.37}_{-0.93}$ kpc. In addition, the velocity dispersion of G23.33-0.30's turbulent velocity component is $\sigma_{shocked} = 2\text{–}5 \, \mathrm{km \, s^{-1}}$, while the velocity dispersions measured toward H II regions in the RAMPS data set (Hogge et al. 2018) are at most $\sigma \lesssim 2 \, \mathrm{km \, s^{-1}}$. Thus, an H II region would need to input an unusually large amount of energy into G23.33-0.30 to reproduce the measured velocity dispersion. Furthermore, $NH_3(3, 3)$ masers have previously only been associated with SNR–MC interactions (McEwen et al. 2016) or energetic outflows from high-mass protostars (Mangum & Wootten 1994; Kraemer & Jackson 1995; Zhang & Ho 1995), so $NH_3(3, 3)$ maser emission resulting from an interaction with an H II region would also be unusual. Consequently, G23.33-0.30's high levels of turbulence are most likely the result of an SNR–MC interaction.

5.3. W41's Potential Impact Geometry

Figure 13 shows that the diameter of W41's shell is much larger than the radial extent of the GMC. If W41's interaction is ongoing and it exploded within G23.0-0.4, then W41's plane-of-sky diameter must be larger than its size along the line of sight. Dense molecular gas can slow or even stall the expansion of an SNR shock into an MC (Tatematsu et al. 1987). Given that MCs can exhibit asymmetric density profiles, core-collapse supernovae shell structures evolving in these environments can also display asymmetries (Lopez et al. 2009). While this is plausible, we might expect W41's expansion out of a dense, massive GMC to sweep up more molecular gas in its shell, whereas this signature is absent in the GRS data. An alternative explanation is that W41's progenitor formed within an MC $\leqslant 20$ pc away from G23.0-0.4. The $82 \, \mathrm{km \, s^{-1}}$ MC shown in Figure 13 could potentially be this cloud. The Reid et al. (2014) near-kinematic distance for $V_{LSR} = 82 \, \mathrm{km \, s^{-1}}$ is $4.60^{+0.26}_{-0.27}$ kpc, consistent with our adopted distance to G23.33-0.30. Although Leahy & Tian (2008) measured a maximum H I absorption velocity of $78 \pm 2 \, \mathrm{km \, s^{-1}}$ toward W41, this may not preclude W41 from also being associated with a background MC. If W41 expanded out of this background MC, the shock may have blueshifted much of the foreground molecular gas that was previously associated with the background MC, confusing the interpretation. Hence, the uncertainty in the origin point of W41's expansion leaves the impact geometry ambiguous.

We have searched for redshifted gas corresponding to the back side of the expanding supernova shell within G23.0-0.4 to help differentiate between these two scenarios. We detected CS emission peaking at $V_{LSR} = 98$ and $103 \, \mathrm{km \, s^{-1}}$, as well as SiO emission peaking at $V_{LSR} = 96 \, \mathrm{km \, s^{-1}}$ near G23.33-0.30, but it is unclear whether this emission is associated with G23.0-0.4 or the interaction. Thus, we examined the GRS ^{13}CO data for signatures of a redshifted component potentially associated with the higher V_{LSR} gas. Although we found emission spanning $V_{LSR} = 93\text{–}106 \, \mathrm{km \, s^{-1}}$ toward the left half of W41, we are hesitant to associate this emission with the back side of

the W41 shell, due to the presence of two background sources. One of these background sources is HMSFR G23.44-0.18, which has a maser parallax distance of $5.88^{+1.37}_{-0.93}$ kpc and $V_{LSR} = 97 \pm 3 \, \mathrm{km \, s^{-1}}$, placing it in the Norma arm near the end of the long bar (Brunthaler et al. 2009; Reid et al. 2014). The second background source is the H II region G23.42-0.21, which seems to contribute much of the continuum emission near W41's left edge (Figure 12). G23.42-0.21 has a recombination line velocity of $103 \, \mathrm{km \, s^{-1}}$ and a maximum H I absorption velocity of $106 \, \mathrm{km \, s^{-1}}$; hence, Leahy & Tian (2008) argued that the absorption velocity was significantly higher than the recombination velocity and that G23.42-0.21 must be assigned to the far distance of ~9.9 kpc.

Considering that there are multiple background sources that confuse the interpretation of any potential redshifted gas, the gas kinematics in G23.33-0.30 may offer additional insight into the interaction geometry. Given that G23.33-0.30 exhibits blueshifted emission as a result of its interaction with W41, W41's progenitor must be behind G23.33-0.30. The details of this interaction also depend on the positions of G23.33-0.30 and W41's progenitor relative to G23.0-0.4. Considering G23.33-0.30's large column density, its apparent position along the spine of the G23.0-0.4, and the necessarily high-mass nature of W41's progenitor, it is plausible that both G23.33-0.30 and W41's progenitor formed near the dense central regions of their natal MCs. If this assumption is valid, then at least two viable scenarios could explain the geometry: either W41's progenitor formed within the GMC and the shock front is perpendicular to the long axis of the filament, or W41's progenitor formed within a background MC and its shock front is roughly parallel with the long axis of the filament. These two scenarios are illustrated in Figures 16 and 17. Unfortunately, neither of these explanations account for the fact that the eastern edge of the filament is more blueshifted than the western edge. If G23.33-0.30 is closer to the edge of the GMC than assumed, the shock could sweep past the bottom edge of the filament more quickly, due to the decreased density on the outskirts of the GMC. Another alternative is that projection effects are confusing our interpretation of the filament's velocity structure. Regardless of the uncertain impact geometry, W41's association with G23.33-0.30's blueshifted gas component and large velocity dispersions is well-founded.

5.4. Possible Negative Feedback from SNR W41

Although shocks from supernovae may drive much of the turbulence in the ISM (Padoan et al. 2016), the influence of these shocks on the star formation process is an open question. Simulations of shock-cloud interactions that include dense substructures demonstrate that the more diffuse molecular gas is efficiently stripped from MCs, while such an impact forms a bow shock around a sufficiently dense molecular core (Patnaude & Fesen 2005). It is possible that the emission deficits in Figure 6 at lower V_{LSR} represent a wake formed behind the cores, which would suggest that some dense gas associated with the cores will remain relatively unperturbed by the passage of the shock. On the other hand, the virial parameters derived from the ^{13}CO emission suggest that the cores are too turbulent to collapse. Furthermore, given that the molecular cores are associated with the intermediately shocked component, they may not yet have experienced as significant an impulse from the shock as compared to the northern section of G23.33-0.30. Indeed, MM3, the core furthest from the
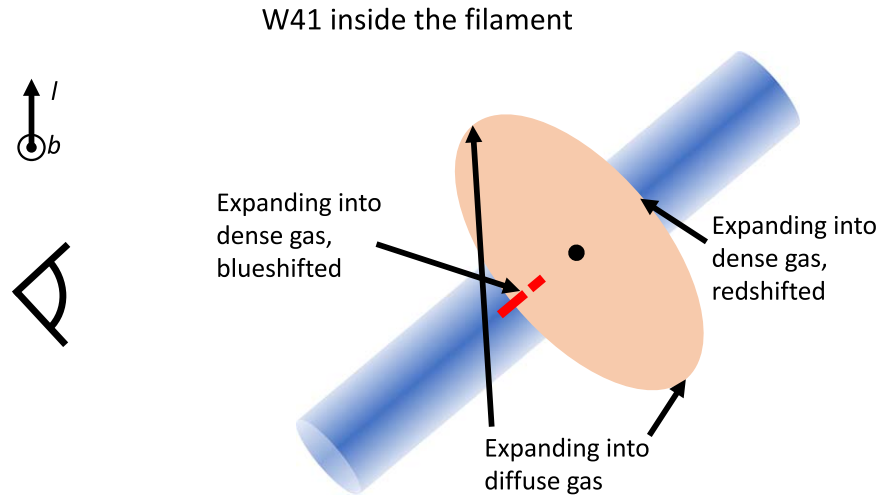
W41 inside the filament

Figure 16. Illustration of top-down view of the scenario in which W41 formed near the center of GMC G23.0-0.4. The figure shows the GMC represented as a blue cylinder, W41's shock bubble as a peach ellipse, G23.33-0.30 as red line segments, and the position of W41's progenitor as a black circle. The filament is rotated in the plane of the Galaxy, such that it roughly matches the orientation of the Reid et al. (2014) Scutum arm, in which the GMC may reside (Brunthaler et al. 2009). Although this model does not depend on the exact orientation of the GMC, some degree of rotation would be required in order to detect blueshifted emission at the location of G23.33-0.30.

W41 outside the filament
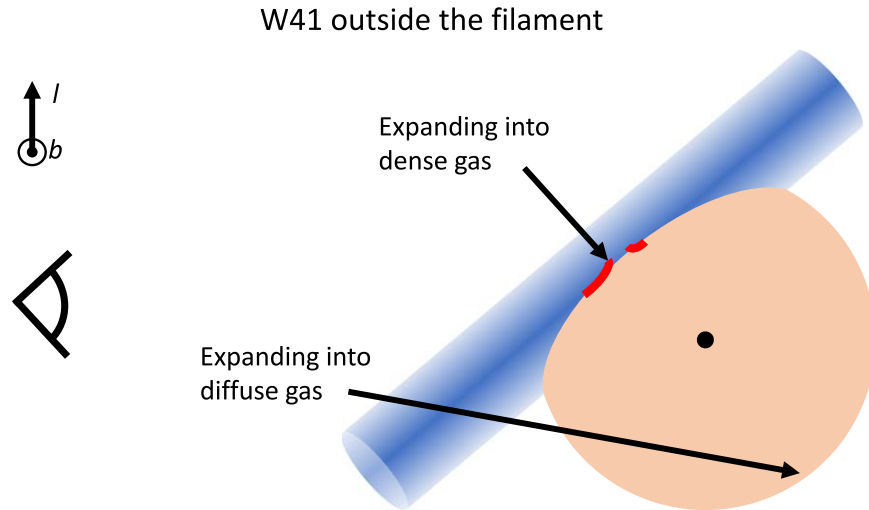
Figure 17. Illustration of top-down view of the scenario in which W41 formed behind GMC G23.0-0.4. The meaning of the shapes is given in the caption of Figure 16.

turbulent component, has the largest $\frac{C^{18}O(2-1)}{^{13}CO(2-1)}$ brightness ratio. This indicates that MM3 has the highest CO(2–1) optical depth, implying that it is also the densest of the cores. If W41's shock passes through the filament and continues to interact with the molecular cores, their velocity dispersions may increase, potentially resulting in the dispersal of the cores. Although we cannot determine whether W41's shock is responsible for the turbulent velocity dispersions of the cores, our data are consistent with negative feedback from the SNR.

6. Conclusion

G23.33-0.30 is a massive IRDC filament that exhibits broad molecular line widths and narrow $NH_3(3, 3)$ line emission. We have imaged the filament using the VLA ($NH_3(1, 1)$ through (6, 6)), the SMA (^{13}CO, $C^{18}O$, 1.3 mm continuum), and the

ACA (SiO(5–4), CS(5–4), 1.3 mm continuum), and we have drawn the following conclusions from our data:

1. We have confirmed the nonthermal nature of three $NH_3(3, 3)$ masers that peak near $V_{LSR} = 56\,\mathrm{km\,s}^{-1}$ and discovered a fourth $NH_3(3, 3)$ maser at $V_{LSR} = 76\,\mathrm{km\,s}^{-1}$.

2. The ACA observations revealed broad SiO(5–4) emission throughout the filament, indicating the presence of a highly turbulent and extended shocked gas component. Because protostellar outflows cannot reproduce the observed SiO emission, high-mass protostellar outflows do not produce G23.33-0.30's $NH_3(3, 3)$ maser emission. The widespread nature of the SiO emission indicates a shock acting on larger scales.

3. The NH_3 emission displays a velocity gradient along the length of the filament, with a significant portion of the filament apparently blueshifted by $\sim$10–17 km s^{-1} with
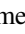
respect to the rest of the filament. G23.33-0.30 also exhibits a velocity discontinuity across the width of the filament, which separates the shocked, turbulent component from the preshock component.

4. Our LTE NH_3 model fitting to the NH_3(1, 1), (2, 2), (4, 4), and (5, 5) data has provided maps of the NH_3 rotational temperature (T_{rot}), velocity dispersion (σ), and LSR velocity (V_{LSR}), which show that the shocked component is blueshifted, hotter, and more turbulent, compared to the preshock component. The correlation among T_{rot}, σ, and V_{LSR} implies that the shock is simultaneously accelerating, heating, and injecting turbulent energy into the shocked filament gas. In addition, the increased ortho-NH_3 abundance inferred from the large $\frac{\Delta T_B(6,6)}{\Delta T_B(5,5)}$ and $\frac{\Delta T_B(6,6)}{\Delta T_B(4,4)}$ brightness temperature ratios imply dust heating.

5. G23.33-0.30 resides within the GMC G23.0-0.4, which previous authors have speculated is undergoing an SNR–MC interaction with W41. Our interferometric data and the GRS ^{13}CO data provide additional evidence of this interaction, which suggests that W41's shock is the common cause for the observed gas kinematics on large and small scales.

6. Although W41's impact geometry remains ambiguous, its interaction with G23.33-0.30 and its plane-of-sky diameter imply that it is at a distance of $d \leqslant 20$ pc from G23.33-0.30.

7. The SMA 1.3 mm continuum data revealed dust cores embedded within G23.33-0.30. Although G23.33-0.30 appears to have sufficient mass ($M \sim 600\,M_\odot$) to form a high-mass star, the observed gas kinematics suggest that the filament is presently being displaced, and potentially dispersed, by the SNR shock. Likewise, our virial analysis ($\alpha = 4$–9) suggests that the cores are also unlikely to collapse. Thus, our data are consistent with negative feedback from the SNR.

ORCID iDs

Taylor G. Hogge https://orcid.org/0000-0002-7211-7078
James M. Jackson https://orcid.org/0000-0002-3466-6164
Andres E. Guzman https://orcid.org/0000-0003-0990-8990
Kathleen E. Kraemer https://orcid.org/0000-0002-2626-7155
Patricio Sanhueza https://orcid.org/0000-0002-7125-7685
Ian W. Stephens https://orcid.org/0000-0003-3017-4418
J. Scott Whitaker https://orcid.org/0000-0001-9179-6312

References

Aharonian, F., Akhperjanian, A. G., Bazer-Bachi, A. R., et al. 2006, ApJ, 636, 777
Albert, J., Aliu, E., Anderhub, H., et al. 2006, ApJL, 638, L101
Anderson, L. D., Bania, T. M., Balser, D. S., et al. 2014, ApJS, 212, 1
Benjamin, R. A., Churchwell, E., Babler, B. L., et al. 2003, PASP, 115, 953
Brogan, C. L., Hunter, T. R., Cyganowski, C. J., et al. 2011, ApJL, 739, L16
Brunthaler, A., Reid, M. J., Menten, K. M., et al. 2009, ApJ, 693, 424
Carey, S. J., Noriega-Crespo, A., Mizuno, D. R., et al. 2009, PASP, 121, 76
Caselli, P., Hartquist, T. W., & Havnes, O. 1997, A&A, 322, 296
Churchwell, E., Babler, B. L., Meade, M. R., et al. 2009, PASP, 121, 213
de Wilt, P., Rowell, G., Walsh, A. J., et al. 2017, MNRAS, 468, 2093
Elitzur, M. 1992, ARA&A, 30, 75
Faure, A., Hily-Blant, P., Le Gal, R., Rist, C., & Pineau des Forêts, G. 2013, ApJL, 770, L2
Foreman-Mackey, D., Hogg, D. W., Lang, D., & Goodman, J. 2013, PASP, 125, 306
Frail, D. A., Claussen, M. J., & Méhault, J. 2013, ApJL, 773, L19
Galván-Madrid, R., Keto, E., Zhang, Q., et al. 2009, ApJ, 706, 1036
Ginsburg, A., & Mirocha, J. 2011, PySpecKit: Python Spectroscopic Toolkit, Astrophysics Source Code Library, ascl:1109.001
Green, D. A. 1991, PASP, 103, 209
Guzmán, A. E., Sanhueza, P., Contreras, Y., et al. 2015, ApJ, 815, 130
Helfand, D. J., Becker, R. H., White, R. L., Fallon, A., & Tuttle, S. 2006, AJ, 131, 2525
H. E. S. S. Collaboration, Abramowski, A., Aharonian, F., et al. 2015, A&A, 574, A27
Hildebrand, R. H. 1983, QJRAS, 24, 267
Hoare, M. G., Purcell, C. R., Churchwell, E. B., et al. 2012, PASP, 124, 939
Hogge, T., Jackson, J., Stephens, I., et al. 2018, ApJS, 237, 27
Hunter, T. R., Brogan, C. L., Indebetouw, R., & Cyganowski, C. J. 2008, ApJ, 680, 1271
Jackson, J. M., Finn, S. C., Chambers, E. T., et al. 2010, ApJL, 719, L185
Jackson, J. M., Rathborne, J. M., Shah, R. Y., et al. 2006, ApJS, 163, 145
Kassim, N. E. 1992, AJ, 103, 943
Killerby-Smith, N. 2018, Review of the Rare NH3(3, 3) Astronomical Masers (Callaghan: Univ. Newcastle)
Kraemer, K. E., & Jackson, J. M. 1995, ApJL, 439, L9
Kroupa, P. 2001, MNRAS, 322, 231
Leahy, D. A., & Tian, W. W. 2008, AJ, 135, 167
Lopez, L. A., Ramirez-Ruiz, E., Badenes, C., et al. 2009, ApJL, 706, L106
MacLaren, I., Richardson, K. M., & Wolfendale, A. W. 1988, ApJ, 333, 821
Mangum, J. G., & Wootten, A. 1994, ApJL, 428, L33
McEwen, B. C., Pihlström, Y. M., & Sjouwerman, L. O. 2016, ApJ, 826, 189
Messineo, M., Menten, K. M., Figer, D. F., et al. 2014, A&A, 569, A20
Misanovic, Z., Kargaltsev, O., & Pavlov, G. G. 2011, ApJ, 735, 33
Molinari, S., Swinyard, B., Bally, J., et al. 2010, PASP, 122, 314
Orlando, S., Peres, G., Reale, F., et al. 2005, A&A, 444, 505
Ossenkopf, V., & Henning, T. 1994, A&A, 291, 943
Padoan, P., Pan, L., Haugbølle, T., & Nordlund, Å. 2016, ApJ, 822, 11
Patnaude, D. J., & Fesen, R. A 2005, ApJ, 633, 240
Peretto, N., Lenfestey, C., Fuller, G. A., et al. 2016, A&A, 590, A72
Pittard, J. M., & Parkin, E. R. 2016, MNRAS, 457, 4470
Rathborne, J. M., Jackson, J. M., & Simon, R. 2006, ApJ, 641, 389
Reach, W. T., Rho, J., & Jarrett, T. H. 2005, ApJ, 618, 297
Reid, M. J., Menten, K. M., Brunthaler, A., et al. 2014, ApJ, 783, 130
Robitaille, T., & Bressert, E. 2012, APLpy: Astronomical Plotting Library in Python, Astrophysics Source Code Library, ascl:1208.017
Sanhueza, P., Jackson, J. M., Foster, J. B., et al. 2012, ApJ, 756, 60
Sanhueza, P., Jackson, J. M., Zhang, Q., et al. 2017, ApJ, 841, 97
Sedov, L. 1959, JApMM, 23, 568
Stil, J. M., Taylor, A. R., Dickey, J. M., et al. 2006, AJ, 132, 1158
Su, Y., Yang, J., Zhou, X., Zhou, P., & Chen, Y. 2014, ApJ, 796, 122
Su, Y., Zhang, S., Shao, X., & Yang, J. 2015, ApJ, 811, 134
Tatematsu, K., Fukui, Y., Nakano, M., et al. 1987, A&A, 184, 279
Tian, W. W., Li, Z., Leahy, D. A., & Wang, Q. D. 2007, ApJL, 657, L25
Umemoto, T., Mikami, H., Yamamoto, S., et al. 1999, ApJL, 525, L105
Urquhart, J. S., Morgan, L. K., Figura, C. C., et al. 2011, MNRAS, 418, 1689
van der Tak, F. F. S., Black, J. H., Schöier, F. L., et al. 2007, A&A, 468, 627
Walch, S., & Naab, T. 2015, MNRAS, 451, 2757

Walmsley, C. M., & Ungerechts, H. 1983, A&A, 122, 164
Walsh, A. J., Breen, S. L., Britton, T., et al. 2011, MNRAS, 416, 1764
Wang, K., Zhang, Q., Wu, Y., Li, H.-B., & Zhang, H. 2012, ApJL, 745, L30
Wardle, M., & Yusef-Zadeh, F. 2002, Sci, 296, 2350
Ward-Thompson, D., Motte, F., & Andre, P. 1999, MNRAS, 305, 143
Zhang, Q., & Ho, P. T. P. 1995, ApJL, 450, L63
Zhang, Q., Hunter, T. R., Sridharan, T. K., et al. 1999, ApJL, 527, L117
Zhang, Q., Wang, Y., Pillai, T., & Rathborne, J. 2009, ApJ, 696, 268